

Transition from Balanced to Unbalanced Motion in the Eastern Tropical Pacific

SAULO M. SOARES,^a SARAH T. GILLE,^a TERESA K. CHERESKIN,^a ERIC FIRING,^b JULES HUMMON,^b AND CESAR B. ROCHA^c

^a *Scripps Institution of Oceanography, University of California, San Diego, La Jolla, California*

^b *Department of Oceanography, School of Ocean and Earth Science and Technology, University of Hawai'i at Mānoa, Honolulu, Hawaii*

^c *Department of Marine Sciences, University of Connecticut, Groton, Connecticut*

(Manuscript received 29 June 2021, in final form 13 April 2022)

ABSTRACT: Kinetic energy associated with inertia–gravity waves (IGWs) and other ageostrophic phenomena often overwhelms kinetic energy due to geostrophic motions for wavelengths on the order of tens of kilometers. Understanding the dependencies of the wavelength at which balanced (geostrophic) variability ceases to be larger than unbalanced variability is important for interpreting high-resolution altimetric data. This wavelength has been termed the transition scale. This study uses acoustic Doppler current profiler (ADCP) data along with auxiliary observations and a numerical model to investigate the transition scale in the eastern tropical Pacific and the mechanisms responsible for its regional and seasonal variations. One-dimensional kinetic energy wavenumber spectra are separated into rotational and divergent components, and subsequently into vortex and wave components. The divergent motions, most likely predominantly IGWs, account for most of the energy at wavelengths less than 100 km. The observed regional and seasonal patterns in the transition scale are consistent with those from a high-resolution global simulation. Observations, however, show weaker seasonality, with only modest wintertime increases in vortex energy. The ADCP-inferred IGW wavenumber spectra suggest that waves with near-inertial frequency dominate the unbalanced variability, while in model output, internal tides strongly influence the wavenumber spectrum. The ADCP-derived transition scales from the eastern tropical Pacific are typically in the 100–200-km range.

KEYWORDS: Pacific Ocean; Tropics; Currents; Eddies; Inertia-gravity waves; Internal waves; Ocean dynamics; Small scale processes; Acoustic measurements/effects; Profilers, oceanic; Ship observations; Spectral analysis/models/distribution; Statistical techniques

1. Introduction

The large-scale circulation of the ocean is strongly influenced by Earth's rotation, which establishes geostrophically balanced flow. At smaller scales, ageostrophic, divergent, wave-like motions dominate ocean currents. The horizontal scale at which the transition from balanced to unbalanced flow occurs is a key factor for understanding observations collected by satellite altimeters, and particularly for interpreting near-surface velocities inferred from the upcoming Surface Water and Ocean Topography (SWOT) satellite altimeter mission (Fu and Uebelmann 2014). SWOT is expected to measure sea surface height (SSH) within the poorly sampled, and poorly understood, submesoscale range (taken here as scales smaller than 100-km wavelength), thus shedding light on the dynamics of these scales through global and systematic sampling (Klein et al. 2019).

Global estimates of this transition scale from a high-resolution numerical simulation vary with season and region

(Qiu et al. 2018). Relatively long scales that lie within the range associated with the mesoscale regime (i.e., longer than 100 km) are found in the tropics. The longer scales contrast sharply with the transition scales found in energetic mid- and high-latitude regimes, also noted in earlier observational studies (e.g., Callies and Ferrari 2013; Bühler et al. 2014; Rocha et al. 2016a; Qiu et al. 2017), implying a reduced range of usefulness for geostrophic currents derived from SWOT in the tropics.

Ocean velocity measurements taken along cruise tracks by acoustic Doppler current profilers (ADCPs) are the primary in situ data that can be used to verify model results (e.g., those in Qiu et al. 2018) and, more broadly, to test hypotheses on the dominant dynamics governing motions in the “submesoscale transition” (approximately the 10–200-km wavelength range, e.g., Chereskin et al. 2019). Previous studies (Bühler et al. 2014; Rocha et al. 2016a; Qiu et al. 2017; Chereskin et al. 2019) of horizontal wavenumber kinetic energy (KE) spectra from ship-board ADCP data found that inertia–gravity waves (IGWs) had significant energy at small scales, flattening the spectra within the submesoscale transition. In mid-to-high latitudes, a high-resolution numerical simulation shows agreement with ADCP results in terms of these spectral characteristics and of the transition scale (Rocha et al. 2016a; Qiu et al. 2017; Chereskin et al. 2019).

Less is known for tropical regions. Qiu et al. (2017) examined ADCP data in the northwest tropical Pacific but did not have in situ data from other tropical regions to evaluate whether the longer transition scale that they found is a

Denotes content that is immediately available upon publication as open access.

Supplemental information related to this paper is available at the Journals Online website: <https://doi.org/10.1175/JPO-D-21-0139.s1>.

Corresponding author: Saulo M. Soares, saulo@ucsd.edu

DOI: 10.1175/JPO-D-21-0139.1

© 2022 American Meteorological Society. For information regarding reuse of this content and general copyright information, consult the AMS Copyright Policy (www.ametsoc.org/PUBSReuseLicenses).

general characteristic of the tropics as implied by the model (i.e., Qiu et al. 2018), or whether it occurs at that location specifically because of low background eddy kinetic energy (EKE), as suggested by the authors. Furthermore, determination of a seasonal signal in KE spectra from ADCPs is challenging because of the small number of independent samples in such datasets (e.g., Chereskin et al. 2019) from the irregular and sparse temporal sampling; so far only limited robust evidence exists for near-surface flows (Callies et al. 2015). Model predictions of strong seasonality in the transition scale and of a strong IGW regime in the submesoscale transition range, therefore, largely lack independent verification.

Our primary goal here is to provide in situ estimates of the balanced and unbalanced components of the KE spectra and of the transition scale in tropical ocean settings. Our secondary goal is to determine if this scale presents seasonal variations, and if such patterns are associated with variations in background mesoscale EKE (e.g., Qiu et al. 2017) or are due to other influences such as mixed layer depth/stratification controls on IGW (e.g., Rocha et al. 2016b) and surface mixed layer instabilities (e.g., Boccaletti et al. 2007; Callies et al. 2015). Finally, we aim to demonstrate that the historical ADCP records are, when carefully processed and analyzed, a key asset to support studies and test hypotheses on the dynamics of the transition from balanced to unbalanced motions and the relative contribution of these motions to SSH signals seen from space.

We focus on three regions in the Pacific Ocean. The first is the northeast tropical Pacific (NETP), where Qiu et al. (2018) found relatively short transition scales with strong seasonality (Figs. 1a,b,c). The second is in the eastern tropical Pacific, just north of the equator, a region referred to as the deep tropics (DTNEP). The third is in the southeast tropical Pacific (SETP; Figs. 1a,d,e), where Qiu et al. (2018) found long transition scales with a weak seasonal cycle. All three regions are well sampled by shipboard ADCP data (Fig. 1a). Our results suggest that the observed KE spectra are often dominated by IGWs such that the ADCP data, in general, support the regional and seasonal patterns seen in the numerical simulation (Qiu et al. 2018) but differ from the model results in a number of details. In particular, the physics governing the transition appears to differ substantially, and differences are region specific. The observations overall suggest that internal tides play a modest role in the surface KE variability and that near-inertial waves dominate the IGW wavenumber spectra of the eastern tropical Pacific. Additionally, they imply that mixed layer instabilities are a likely cause of the weak and region-specific seasonality in the balanced spectra; the divergent, would-be IGW spectra, in contrast, show no seasonality.

The paper proceeds with the details of the methods and datasets (section 2), followed by the main results: the area-averaged spectral characteristics and their decomposition into rotational and divergent as well as wave and vortex components (section 3). Subsequent sections address the robustness of our estimates and discuss their caveats and broad implications. The paper ends with a summary of key points and concluding remarks. For completeness, a detailed recap of the

decomposition method and additional supporting figures appear within the supplemental material.

2. Methods and data

a. Inferring dynamics from one-dimensional horizontal wavenumber spectra

The spectral slopes and power ratios between the components of horizontal KE wavenumber spectra, together with their depth dependence, are useful diagnostics that may indicate the presence of certain dynamical regimes (e.g., Callies and Ferrari 2013). For isotropic flows, either purely rotational or divergent, the power-ratio between the cross- and along-track components is directly proportional to the KE spectral slope. Dominantly rotational motions, such as in a quasi-geostrophy (QG) turbulence regime (e.g., interior QG; Charney 1971), project primarily onto the cross-track component. Predominantly along-track energy would be indicative of divergent, ageostrophic motions (Callies and Ferrari 2013), which may include a variety of phenomena with differing dynamics (IGWs, mixed layer instabilities, fronts and filaments, etc.). For flows that contain both nondivergent and divergent components, there are no set expectations for the power ratio between the cross- and along-track components of KE, nor for its connection to the KE spectral slope.

Besides interpretation of the above two spectral properties and their relationship, we use the two-step decomposition method of Bühler et al. (2014) to obtain both the rotational and divergent spectral components (aka Helmholtz decomposition), as well as the vortex (balanced) and wave (IGW) components of the KE spectra. This method allows a better dynamical diagnostic. A similar approach has been used for atmospheric flight-track data (Lindborg 2007, 2015).

The Bühler et al. (2014) decomposition has strict assumptions, namely, that the rotational and divergent fields are stationary, homogeneous, isotropic random functions. While the isotropy assumption can be relaxed under specific circumstances (see Bühler et al. 2017), a one-dimensional (1D) Helmholtz decomposition can be made without assuming anything about the relationship between the rotational and divergent fields (see supplement text and Lindborg 2015). The vortex-wave decomposition of KE further assumes that IGWs obey the Garrett and Munk (1972, GM) spectrum or a similar model (e.g., Levine 2002, hereafter L02). This last step also assumes that all divergence is solely provided by linear IGWs that propagate in a horizontally uniform background stratification that varies slowly in the vertical, consistent with the WKB approximation. We implement the method according to the steps outlined in appendix C of Rocha et al. (2016a), relying on the exact solution of the coupled ordinary differential equation (ODE) pair proposed by Bühler et al. (2014).

This decomposition is a statistical tool: it requires a sufficiently large number of ensemble members in order to yield robust along-track and cross-track velocity spectra. Even when confidence limits suggest that derived quantities such as the transition scale are valid, they must be interpreted cautiously, particularly at the extremes of the spectrum, e.g., near the

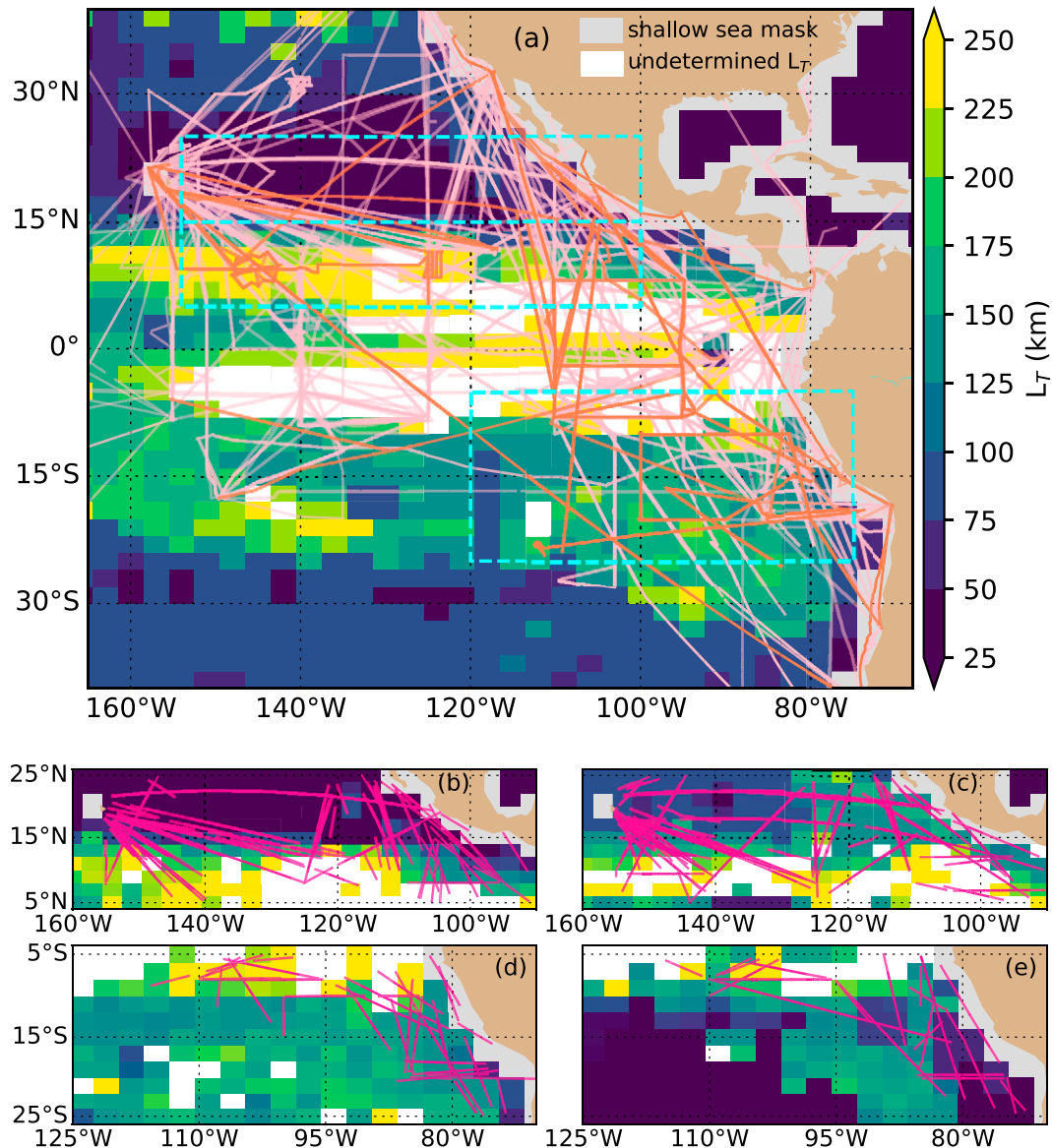


FIG. 1. Transition scale (L_T) from the LLC4320 simulation overlain with cruise tracks. data on L_T from [Qiu et al. \(2018\)](#). (a) Annual mean L_T overlain with ship/cruise tracks from the JASADCP (pink lines) and R2R (orange lines) repositories; the boxes delimited by cyan dashed lines show the three averaging domains. LLC4320 L_T for (b),(c) the northeast/deep tropical Pacific and (d),(e) the southeast tropical Pacific during FMA (boreal winter/spring) in (b) and (d), and during ASO (boreal summer/fall) in (c) and (e); magenta lines show the 500-km transects used for each season as defined in [section 3c](#). White pixels denote areas where L_T exceeds 500 km; light gray areas denote a shallow sea mask.

Nyquist wavenumber or at the lowest resolvable wavenumber. To apply this approach to ship tracks with wide spatial coverage ([Fig. 1](#)), we assume that the statistics of the velocity spectra are homogeneous within an area larger than the transect lengths over which spectra are calculated.

b. ADCP data

We use ADCP data from two repositories: 1) the Joint Archive of Shipboard ADCP data (JASADCP) and 2) the

Rolling Deck to Repository (R2R) shipboard ADCP collection housed at the National Centers for Environmental Information (NCEI). While JASADCP contains only ready-to-use ADCP cruise data (processed largely with University of Hawaii software and methods, see [Firing and Hummon 2010](#)), the NCEI repository contains a large amount of unprocessed ADCP data, including many uninterrupted science-free transits. Processed ADCP cruise data consist of vertical profiles of ocean velocity relative to the sea floor, averaged over some

time interval, typically 2–5 min, and organized in discrete depth bins. The two repositories were searched for underway ship transects within the regions of interest that were collected with minimal interruptions (e.g., for hydrographic stations) and sufficiently fast, meaning with an average ship speed above $\sim 3.5 \text{ m s}^{-1}$, an upper bound of speed of the first baroclinic mode. As part of our study, previously unprocessed cruises were processed with UHDAS (University of Hawaii Data Acquisition System) software, permission was sought as needed to release proprietary data, and data were archived at JASADCP. The resulting dataset is more temporally and geographically diverse than data used in previous studies (see ship tracks in Fig. 1). The set constitutes a blend of sonar types under various profiling configurations (e.g., pulse length, ping frequency, blanking interval, averaging interval) that affect depth range and resolution as well as accuracy and horizontal resolution. The list of cruises used in this study is in Table S1 in the online supplemental material.

This analysis focuses on the near surface, using the bin centered nearest to 30-m depth. To minimize potential near-field artifacts, we discard data from the top two bins. We also preferentially select high-frequency sonars and/or sonars operating in broadband mode when available, yielding typical bin widths of 2–8 m, narrow enough to afford a detailed view of the upper ocean. The 30-m depth bin emerges as a good compromise between data quantity, quality, and surface proximity.

We analyze data collected from 1994 to 2018. These vary in quality mostly because, prior to the early 2000s, data acquisition systems and processing techniques limited ping-data screening and editing capabilities. During the 1990s, not only were GPS fixes sparser, but signals for civilian use were dithered [known as selective availability (SA)] to lower accuracy. However, we found older data, in general, to be adequate for our purposes, with statistics that differ little from the more modern data, possibly reflecting the fact that most ships were equipped with P (Precise) code GPS, which bypassed SA. We also have not found evidence that sonar type, frequency, or configurations affect the spectral characteristics of the data in a systematic manner other than shifting noise levels at the highest wavenumbers, corresponding to scales shorter than 10 km.

The data treatment is as follows. We analyze 256 mostly uninterrupted and gap-free transects (no gap larger than 20 km, no more than 10% small gap coverage) that are at least 500 km long, drawn from our blended dataset. Small gaps are filled through linear interpolation. Each transect is visually inspected for possible issues that might have escaped quality control procedures or that were not resolvable by prior processing, and any transects deemed contaminated are discarded; for this study we discarded three transects because of suspect data. Transects that pass screening are then block-averaged to a 2-km regularly spaced grid.

To calculate KE spectra, we first subdivide transects into 500-km-long segments, with 50% overlap between segments (when transects exceed 750 km in length). This length yields sufficient ensemble members to produce sensible averages and allows us to resolve wavelengths between $\sim 167 \text{ km}$

(corresponding to 3 cycles per record length, the lowest wavenumber free of windowing effects) and 4 km, our Nyquist wavelength. Segments that deviate from a geodesic by more than 2% are discarded. Prior to forming spectral estimates, the velocities are rotated into an along- and cross-track coordinate system based on the segment's median ship velocity vector. All velocity components are then detrended and windowed with a Blackman–Harris window (setting effective degrees of freedom to 1.98 times the total number of segments, determined according to Percival and Walden 1993). As in Rocha et al. (2016a), results are not sensitive to the choice of window. We obtain the KE wavenumber spectrum of each segment by Fourier transforming these velocities, multiplying the Fourier coefficients by their complex conjugates, and then correcting the spectral variance for the windowing. Finally, robust spectral estimates are formed by averaging specific segments together, with confidence limits estimated assuming that the Fourier coefficients are normally distributed and that their magnitudes squared follow a χ^2 distribution (Bendat and Piersol 2010). Uncertainties for the Helmholtz decomposition are estimated by propagating the upper and lower limits of the KE spectral confidence limits.

As in previous studies, we use the fast-tow assumption, treating the data as if the ships sampled the 500-km segments instantaneously. In reality 18–30 h are required, so wavenumber estimates are Doppler shifted. This issue is discussed in section 6b; other less common sampling and measurement issues are left for a future article.

c. Ancillary data

1) HYDROGRAPHIC DATA

We use vertical profiles of in situ temperature and salinity to estimate monthly and seasonal averages of mixed layer depth and of full-depth profiles of buoyancy frequency (N) along ship transects. The mixed layer depth is used to determine whether the 30-m ADCP bin is within the mixed layer or the stratified transition layer at the top of the thermocline. The N profiles are employed primarily to generate the GM horizontal wavenumber spectra required by the wave–vortex decomposition (Bühler et al. 2014; Rocha et al. 2016a).

From the World Ocean Database 2018 (WOD; Boyer et al. 2019), we take only high-resolution (5 dbar or less in the upper 1000 m), high-quality (with WOD quality flag accepted) in situ temperature and salinity measured by shipboard CTD casts and Argo floats for the period 1994–2018, within the three regions of interest. Profiles are organized by month. For each calendar month, we keep only profiles within 125 km of the center position of available segments and profiles separated by at least 7 days, to minimize correlation between samples and biases in the mean. The mixed layer depth for each profile is estimated using a threshold method by seeking the first pressure where the potential density is larger than that of the uppermost bin by 0.03 kg m^{-3} , a value roughly proportional to a temperature change of 0.2°C (de Boyer Montégut et al. 2004). We calculate $N^2(z)$ directly using profile data in native pressure bins. Each N^2 profile is then interpolated to standard depths, and we compute the median and the 95%

and 5% quantiles from all valid profiles in the vicinity of the tracks. The range from these quantiles is used as the uncertainty for N . For the mixed layer depths, we compute the mean and standard deviation of the valid profiles; the standard deviation is taken as the sampling uncertainty. For each domain, we calculate a climatological seasonal cycle of mixed layer depth from the monthly averages of these ship-track means, and we bound the cycle's uncertainty by propagating the sampling uncertainty.

2) HIGH-RESOLUTION GLOBAL SIMULATION

We use output from a global numerical simulation with the Massachusetts Institute of Technology general circulation model (MITgcm; Marshall et al. 1997) known as LLC4320 (LLC stands for latitude–longitude cap; Forget et al. 2015). Details of the LLC4320 and its parent simulations can be found in Rocha et al. (2016a,b), Qiu et al. (2018), and Menemenlis et al. (2008). This high-resolution simulation produced more realistic submesoscale dynamics, including an IGW continuum (Nelson et al. 2020). The output, which has a grid spacing of $1/48^\circ$, is available as hourly snapshots. We analyzed a 1-yr period between 1 November 2011 and 31 October 2012, which is roughly the same as others have analyzed (Rocha et al. 2016b; Qiu et al. 2018).

The model analysis provides a comparison point for the ADCP results. Within our study domain, we extract weekly surface current snapshots along model grid lines spaced at 2.5° increments in latitude/longitude. Spectral calculations follow the same procedure as those for the ADCP, using 50% overlapping 500-km-long segments regridded to have uniform 2-km sampling. The Helmholtz and wave–vortex decompositions are then applied to the area-averaged spectra. This wave–vortex decomposition uses the GM model with parameters from the observed stratification to be consistent with the ADCP treatment.

We also perform experiments with the model output in order to establish the influence of sampling on the spectral estimates. For these tests, weekly output is interpolated linearly onto the ship tracks taken directly from the final, cleaned, segmented ADCP database, i.e., tracks already evenly spaced at 2-km resolution. This analysis uses two-dimensional latitude/longitude interpolation only and is not intended to replicate the details of ship sampling (e.g., time variability aliasing). We test two geographical track configurations: one using all the available tracks, yielding a dense sampling pattern, and one using a subset of the tracks, yielding sparser coverage. Last, we sample each week using only the tracks associated with that month, in order to mimic a more realistic geographical and seasonal sparse sampling.

3) GRIDDED ALTIMETRY-DERIVED GEOSTROPHIC CURRENTS

We use surface absolute geostrophic currents from the Sea Level Thematic Center (SL-TAC) delayed time product available on a $1/4^\circ$ grid at daily intervals. The data are available through Copernicus Marine Environment Monitoring Service (CMEMS). We consider data for the period 1993–2018

and calculate the eddy kinetic energy (EKE) by applying a bandpass filter with a moving window length of 10–120 days and a 100-km-wide Gaussian spatial smoother. These data are used to determine if there is a seasonal cycle of background EKE for the areas of interest and to evaluate whether any such cycle is related to the ADCP-derived spectral estimates. We focus on area-weighted means of the filtered data and average only grid points visited by the ship tracks. A composite seasonal cycle of EKE is formed by monthly averaging the area-means and then averaging over the record. To better understand the LLC4320 simulation, we single out the year 2011/12 and calculate its EKE anomalies relative to the multiyear climatology. Uncertainty is given by the standard error of the mean, propagating the spatial standard errors (after accounting for spatial correlation) through the monthly (where only every 10 days is considered independent) and climatological averaging.

3. Results from the ADCP and ancillary observations

a. Regional annual-mean spectra

The KE spectra and their cross- and along-track components are aggregated by month and averaged within each of the three domains shown in Fig. 1. To avoid biasing the means, given the likely existence of seasonality (as discussed below), we use the following strategy: we retain the same number of segments for each season (where the year is split into two seasons, defined as consecutive 6-month periods), discarding excess data from oversampled months while at the same time attempting to maintain consistent geographical coverage during the two periods (thus also discarding samples from isolated areas that were not sampled in other months). The annual mean along- and cross-track components of the KE spectra are displayed in Figs. 2a–c.

In the NETP the KE spectra roll off with a least-squares-fit slope of -2.15 ± 0.1 from 15 to 200 km (Fig. 2a). The power ratio between the cross- (\hat{C}^v) and along- (\hat{C}^u) track components is only consistent with the slope for low wavenumbers, where it has a value near 2, and thus indicates that geostrophic dynamics dominate at scales larger than 100 km. The power ratio quickly decreases to one at around 30-km wavelength and then to about 0.9 for the remainder of the high wavenumber band, indicative of a loss of geostrophic balance. In the DTNEP, the KE spectra appear to be slightly flatter (-1.95 ± 0.1 slope), and in the SETP they are flatter still (-1.8 ± 0.12) for the 15–200-km wavelength range (Figs. 2b,c). The power ratio at the lowest resolvable wavenumber (~ 170 km) is 1.8 for the DTNEP and 1.4 for the SETP. Hence, consistency with geostrophy appears only at these very large scales as well. The power ratio then sharply decreases to one at about 60–70-km wavelength and then decreases again relatively more slowly (relative to what was observed in the NETP) to about 0.8 for both these regions. The slope of the cross-track component is slightly steeper than the along-track component in all regions, hence driving most of the ratio changes.

Overall, the KE spectra differ significantly between the three regions mainly for scales ≥ 50 km, with higher levels of

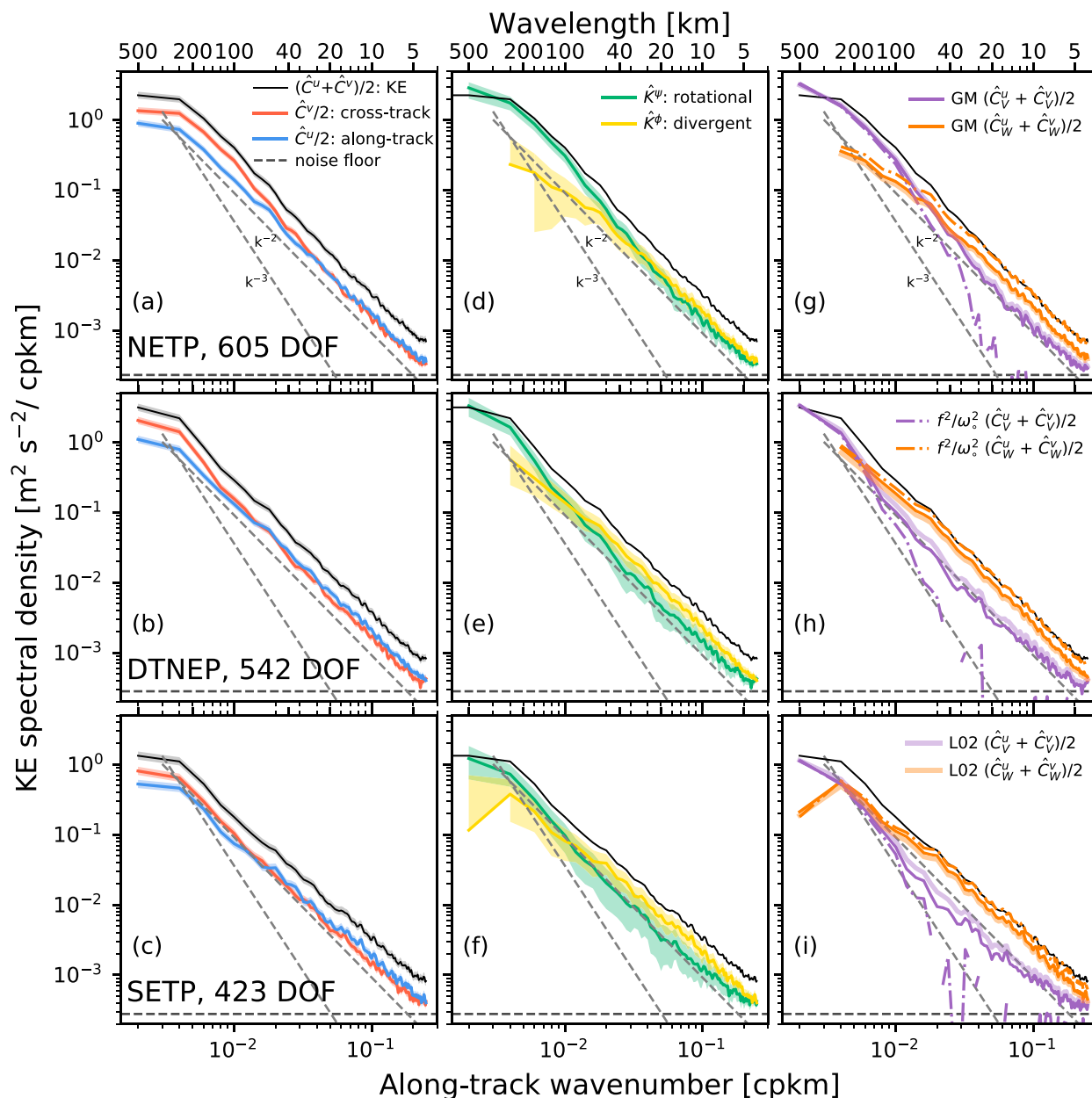


FIG. 2. Annual-mean spectra of kinetic energy (KE, thin black lines), and the cross- (\hat{C}^v , red lines) and along-track (\hat{C}^u , blue lines) components, for ADCP data collected in (a) the northeast tropical Pacific, (b) the deep tropical northeast Pacific, and (c) the southeast tropical Pacific. (d)–(f) Corresponding Helmholtz decomposition of the KE spectra into rotational (\hat{K}^ψ , green lines) and divergent (\hat{K}^ϕ , yellow lines) parts. (g)–(i) The partition of KE into wave (KE_W , orange lines) and vortex (KE_V , purple lines) components, using the Garrett–Munk (GM) spectrum (thin dark lines), Levine (L02) spectrum (thick light lines), and a constant f^2/ω^2 (values for each region shown in Fig. 3). Shading denotes the 95% confidence interval. Negative spectral energy levels are masked. Dashed lines show the noise floor (black, see the appendix) and the reference k^{-2} and k^{-3} curves (gray). In-panel labels are applicable column wise.

energy in the NETP and DTNEP relative to the SETP. In general, the regional differences are larger for the cross-track component of KE (red lines in Figs. 2a–c), with more energy at most wavenumbers in the NETP, followed by the DTNEP and then by the SETP. The along-track component is also less energetic at low wavenumbers in the SETP (Fig. 2c) when compared with the two other regions, contributing to the lower levels of KE in

this region. Below scales of 40–50 km, the along-track component spectra in all three regions are nearly identical. At scales ≤ 15 km, the cross-track spectra in all three regions are nearly identical, and we note further flattening at these very high wavenumbers (scales ≤ 15 –5 km) for this component, which we attribute to noise. This noise effect leads to an artificial increase in the power ratio at very high wavenumbers.

The Helmholtz-decomposed spectra are shown in Figs. 2d–f. The rotational component (K^{ψ}) clearly dominates the divergent component (K^{ϕ}) only for scales ≥ 70 km in the NETP (Fig. 2d), and ≥ 200 km for the DTNEP and SETP (Fig. 2e,f). For the SETP, this dominance is less reliable (note the overlapping shading in Fig. 2f). In the NETP, K^{ψ} and K^{ϕ} contribute equally around 30-km wavelength (Fig. 2d). The divergent component slightly dominates the rotational component for smaller scales. In the DTNEP and SETP, the divergent component starts to dominate at scales of about 80 km, with a larger ratio of divergence to rotation seen in the SETP than in the DTNEP, and much larger still than seen in the NETP. This dominance means that K^{ϕ} typically represents 60%–70% of the KE at these scales, and this fraction is much larger than what has been reported elsewhere, except by Qiu et al. (2017) in a small area of the western tropical Pacific. In the NETP and DTNEP, the spectra of K^{ψ} appear to roll off as $k^{-2.5}$ between 20- and 200-km scales.

In Figs. 2d–f, the small rise in rotational energy for scales smaller than ~ 10 km is ascribable to noise. This illustrates that even modest levels of (mostly white) noise can impact the accuracy of the Helmholtz decomposition at high wavenumbers. Because the Helmholtz decomposition depends on the differences in power between the cross- and along-track components, the rotational and divergent components are more uncertain (see shading in Figs. 2d–f) than the cross-track and along-track components (Figs. 2a–c).

The results in Figs. 2d–f show that in the submesoscale-transition range, ageostrophic and divergent motions are important for the NETP and are likely dominant in the DTNEP and SETP regions of the eastern tropical Pacific. With spectral slopes flatter than -3 , interior QG does not appear to be the most relevant framework to interpret the total KE. The spectra do not display the signature characteristics of surface quasigeostrophy (SQG; Blumen 1978) described by Callies and Ferrari (2013) such as flattening at scales longer than the injection scale (estimated here to be at 10–30 km), or abrupt steepening with depth (Fig. S1), indicating that SQG is unlikely to explain the observed KE. Other frameworks for balanced dynamics, e.g., those originating from mixed layer baroclinic instabilities (Callies et al. 2016; Cao et al. 2021), may still be relevant to interpret the spectra, particularly in the NETP, where rotational energy is comparable to divergent energy over many smaller scales. This evaluation, however, will require isolating the balanced component, since many ageostrophic flows also have a rotational component. The easiest case to analyze with 1D data is a flow composed of only linear IGWs and nondivergent eddies.

b. The wave–vortex decomposition and the transition scale

To separate wave and vortex contributions to the KE with the Bühler et al. (2014) method, we require knowledge of the frequency content of the IGW field. This knowledge is encapsulated by the empirical parameter $f^2/\omega_*^2(k)$, which is related to the ratio $\hat{C}_{\psi}^{\psi}/\hat{C}_{\psi}^{\phi}$, where \hat{C}_{ψ}^{ψ} is the spectrum of the divergent cross-track velocity of the wave component and \hat{C}_{ψ}^{ψ}

its rotational along-track velocity component. Following Bühler et al. (2014), an external model of IGW energy is used to determine $f^2/\omega_*^2(k)$, the squared ratio of the local inertial frequency f to a wavenumber-dependent frequency function ω_* . This yields the unknown \hat{C}_{ψ}^{ψ} , under the assumption that all of the divergent energy is due to IGWs, i.e., that $\hat{C}_{\psi}^{\psi} = \hat{C}_{\psi}^{\phi}$, where \hat{C}_{ψ}^{ϕ} is the spectrum of the divergent cross-track velocity from the Helmholtz decomposition. Isotropy determines \hat{C}_{ψ}^{ψ} and thus the wave KE, and the vortex KE is found by subtracting the wave from the total KE. We use the GM model and the L02 version of GM to estimate $f^2/\omega_*^2(k)$ as part of an evaluation of the sensitivity of the wave–vortex decomposition. This is possible because of the energy equipartition property of IGWs (Bühler et al. 2014). The L02 formulation shows a better fit to frequency spectra in the tropics (L02; Polzin and Lvov 2011).

We first explore the sensitivity of f^2/ω_*^2 to specific formulations and parameter choices of the IGW models. Parameters for the GM model were obtained from exponential fits to the N profiles shown in Figs. 3a–c and are tabulated in Table 2. The L02 model uses the observed N profiles in Figs. 3a–c. The calculations are carried out between 4000 and 30 m, the depth at which most of our ADCP data were measured. We show f^2/ω_*^2 predictions for the GM and L02 models in Figs. 3d–f (gray lines), for annual mean, winter/spring, and summer/fall stratification conditions. In all three domains the L02 model predicts smaller ratios at all wavenumbers. The differences result almost entirely from the shape of the L02 frequency spectrum. Stratification has little impact on model ratios; sensitivity tests show that these models require much larger variations of N with depth than are observed either seasonally or even regionally, in order to impact the IGW behavior near the surface (as indicated by the thin, often superimposed, gray lines in Figs. 3d–f).

There is also an alternative approach. In a regime where wave energy dominates, $\hat{C}_{\psi}^{\psi}/\hat{C}_{\psi}^{\phi}$ from the Helmholtz decomposition is directly comparable to f^2/ω_*^2 , and is thus a useful test for an IGW model. For ADCP spectra, this would occur for scales less than 40 km for the NETP (Fig. 2d) and for scales less than 100 km for the DTNEP (Fig. 2e) and SETP (Fig. 2f). In this IGW regime, regardless of season, ADCP-derived $\hat{C}_{\psi}^{\psi}/\hat{C}_{\psi}^{\phi}$ (colored lines in Figs. 3d–f) plateaus between 0.5 and 0.8 depending on the region, before increasing again at high wavenumbers presumably due to a combination of noise and the boundary condition of the method (Rocha et al. 2016a, or the supplemental text).

The fact that $\hat{C}_{\psi}^{\psi}/\hat{C}_{\psi}^{\phi}$ ratios do not converge to the GM or L02 predictions implies that the IGW models may have shortcomings. Additionally, the high ratio specifically implies that the observations are dominated by near-inertial-like IGWs. This result argues for the use of a narrowband wave–vortex decomposition prescribed by a constant f^2/ω_*^2 (dash-dotted lines in Figs. 2g–i for annual-mean KE wave–vortex decomposition). In all regions, the use of f^2/ω_*^2 in lieu of a wave model leads to a larger wave to vortex KE ratio and results in steeper spectra for KE_v (Figs. 2g–i). This contrasts with the lower sensitivity of the wave–vortex partition when choosing

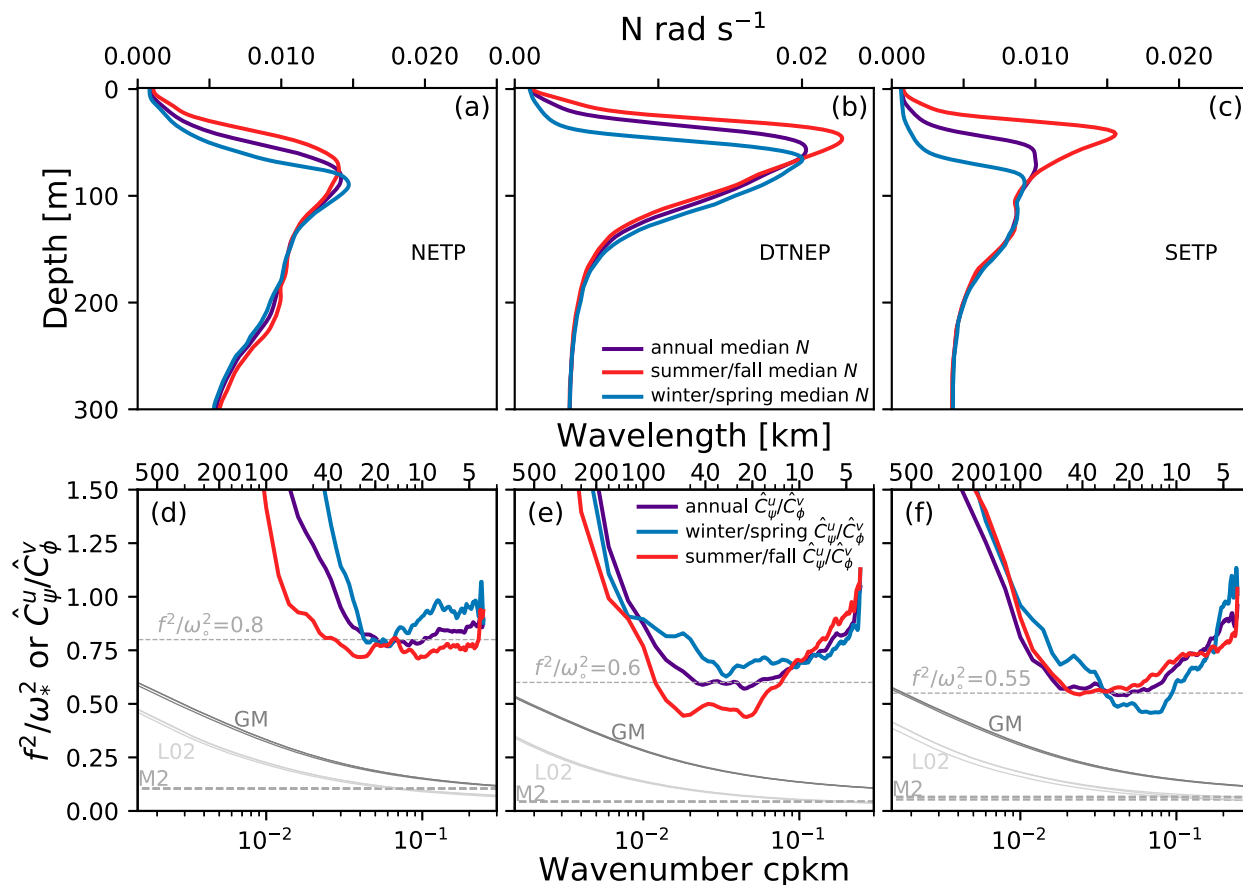


FIG. 3. (a)–(c) Buoyancy frequency (N) observed in the vicinity of the cruise transects used for each averaging domain; annual mean (indigo lines), winter/spring (blue) and summer/fall means (red) are shown. (d)–(f) The ratio of \hat{C}_ψ^u to \hat{C}_ϕ^v , which is equivalent to f^2/ω_*^2 , derived from the Helmholtz decomposition of ADCP data in each domain, color-coded by season; also shown are f^2/ω_*^2 predictions by the Garrett–Munk (GM, dark gray) and Levine (L02, light gray) spectral models for the various N profiles, along with the values for the M_2 internal tide and for the frequency ω_* that best matches the observed ratio.

between the GM or L02 models (solid lines in Figs. 2g–i). Differences between the narrowband ω_* and broadband ω_* estimates are as large as, and at times exceed, the uncertainty range obtained by propagating the statistical uncertainty through the wave–vortex step (the shading is omitted in Figs. 2g–i and 5c,d for clarity).

Overall, our analysis indicates that in the eastern tropical Pacific, IGWs account for $\sim 70\%$ of the annual-mean total KE (and hence most or even all of the shape of the spectra) below a certain scale (which is domain dependent) (Figs. 2g–i). This generally holds whether using f^2/ω_*^2 or the GM model, with the former method implying larger fractions of wave KE and weaker, steeper vortex spectra. Following previous work (Qiu et al. 2017; Chereskin et al. 2019), we define the transition scale from balanced to unbalanced motions as the KE_W and KE_V crossover wavelength in the wave–vortex decomposition (e.g., the scale at which the purple line is equal to the orange line in Figs. 2g–i). The transition scale, as summarized in Table 1, is shorter in the NETP, where it is 50–100 km, is around 200 km in the DTNEP, and is longest in the SETP. The

narrowband IGW model yields longer transition scales than broadband IGW models such as GM, but the choice of GM versus L02 does not impact the transition scale.

c. Seasonality in spectra and transition scale

The KE spectra and their wave–vortex partitioning often exhibit time variability in the form of seasonality (Callies et al. 2015; Rocha et al. 2016b; Qiu et al. 2017, 2018). Whereas the area-averaged mixed layer depth undergoes a well-defined seasonal cycle in all regions, with deeper layers in winter/spring than in summer/fall (Table 2), background EKE does not display much seasonality (Table 2). The background EKE has larger interannual than seasonal variability; however, we lack sufficient ADCP data to resolve the former. To explore seasonality in the ADCP spectra and transition scales, we define seasons using the mixed layer depth and contrast the spectra, Helmholtz decompositions, and wave–vortex decompositions for July–October with those for January–April (December–March for the NETP, Figs. 4 and 5).

In all three regions, ADCP energy levels in winter/spring spectra differ slightly from summer/fall spectra, but only in

TABLE 1. Transition scale estimates from wave–vortex decomposition (km). For ADCP-derived scales, the range shows estimates using the Garrett–Munk (GM) model (low values) and narrowband model (high values). The LLC4320-derived scales in this study use the 1D method with the GM model only for zonal transects and ship transects (in parentheses). The LLC4320 scales obtained by Qiu et al. (2018) (Fig. 1) were averaged in the three domains, where values in parenthesis only average areas visited by ship tracks. The asterisk denotes that the scales are underestimated in the DTNEP and SETP because undefined values (white pixels in Fig. 1) are set to 500 km.

	NETP	DTNEP	SETP
ADCP annual	65–90	170–200	190–240
LLC4320 annual	110 (100)	>500 (265)	250 (250)
Qiu18 annual*	40	270 (250)	210 (230)
ADCP winter/spring	35–90	190–230	190–210
ADCP summer/fall	90–110	250–264	300
LLC4320 DJFM	45 (90)	>500 (235)	230 (230)
LLC4320 JASO	170 (180)	>500 (460)	240 (300)
Qiu18 FMA*	27 (43)	300 (270)	230 (215)
Qiu18 ASO*	113 (112)	330 (315)	130 (180)

the NETP are the differences significant at the 95% level (Fig. 4a and Fig. S2). We find no significant differences in slope between seasons in all regions. In the NETP, there is a substantial increase in KE at scales less than 100 km (Fig. 4a) in winter/spring relative to summer/fall, but this contrast is absent elsewhere. Hence, we focus solely on the NETP here. At the longest scales, the along-track component of KE (Fig. 4c) accounts for most of this energy increase, yielding a power ratio near one at these scales. For scales less than about 100 km the cross-track component (Fig. 4b) contributes more for the seasonal increase than the along-track.

Divergence energy in winter/spring is similar to summer/fall for most wavenumbers (but weaker at larger scales, Fig. 5b). The seasonal increase in KE for scales less than 100 km is driven by the rotational component (Fig. 5a). In winter/spring, \hat{K}^ψ is flatter than in summer/fall, and the scale at which \hat{K}^ψ equals \hat{K}^ϕ decreases, from 40 km in summer/fall to 20 km in winter/spring. Unlike the directly observed KE components, the seasonal changes in the energy density of the Helmholtz

components are highly uncertain. Further decomposition into wave and vortex KE (Figs. 5c,d) suggests that IGWs undergo little seasonality, regardless of the IGW model used, with substantial changes only at the largest scales, which we discuss in section 6.

Statistical reliability of the decompositions aside, we find a pronounced seasonality in the vortex KE component, with seasonal vortex KE differences found for both IGW models for scales below ~150 km. The winter/spring vortex KE spectrum appears to be slightly flatter than the summer/fall spectrum, at least for scales longer than ~50 km (cf. dark and light purple lines in Figs. 5c,d). The use of the narrowband near-inertial model to perform the decomposition results in a noticeably steeper summer/fall vortex spectrum (Fig. 5d).

The estimates for the transition scale for each region and season are shown in Table 1. The scale shortens only slightly during winter/spring in the NETP, but lengthens considerably during summer/fall; the precise scale and its seasonal amplitude depends again on the type of IGW model. The transition scale in the NETP, in any case, is expected to be no more than 100 km. The seasonality in this transition is due to the increase in vortical KE at scales of 50–100 km. In determining the NETP winter/spring transition scale for the narrowband method, we ignore the crossover of the vortex and wave KE spectra at the largest scales (Fig. 5d); in section 6 we discuss why we do not consider the large-scale elevated along-track variance to be exactly IGW related. In the SETP and DTNEP, the transition scale in both seasons remains much longer than in the NETP, at or above 200 km (increasing in summer/fall but unreliably), and depends little on the choice of IGW model. This results from the year-round dominance of IGWs, which undergo weak or nonexistent seasonality (e.g., Fig. S2).

In the three regions considered here, seasonal changes in stratification are confined to the upper 150 m, with the amplitude of the seasonal signal quickly decreasing with depth (Figs. 3a–c). The cycle is relatively small in the NETP and is more pronounced in the DTNEP and SETP, where summer/fall N increases by nearly an order of magnitude. This provides an explanation for the low seasonality in IGW KE near the surface for the NETP. It seems inconsistent with the weak

TABLE 2. Parameters used in the Garrett–Munk model of IGW energy, and domain-averaged values for mixed layer depth (MLD) from Argo data and background mesoscale eddy kinetic energy (EKE) from gridded altimetry data. The latitude used is the mean latitude of the selected ship tracks; see section 3b for details on the calculation of the other parameters.

	Latitude (°)	N_0 (s ⁻¹)	b (m)	MLD (m)	EKE (m ² s ⁻²)
NETP					
Annual	18.4	10.3×10^{-3}	804	44 ± 8	$1.05 \times 10^{-2} \pm 5\%$
Winter/spring	18.1	10.2×10^{-3}	807	51 ± 9	$1.02 \times 10^{-2} \pm 5\%$
Summer/fall	18.0	10.3×10^{-3}	810	35 ± 6	$1.08 \times 10^{-2} \pm 5\%$
DTNEP					
Annual	11.4	9.1×10^{-3}	872	34 ± 4	$2.42 \times 10^{-2} \pm 6\%$
Winter/spring	11.7	9.5×10^{-3}	853	43 ± 4	$2.78 \times 10^{-2} \pm 6\%$
Summer/fall	11.8	8.9×10^{-3}	890	25 ± 4	$2.16 \times 10^{-2} \pm 5\%$
SETP					
Annual	−12.8	7.2×10^{-3}	1005	52 ± 8	$5.41 \times 10^{-3} \pm 5\%$
Winter/spring	−14.0	6.8×10^{-3}	1043	77 ± 10	$5.80 \times 10^{-3} \pm 5\%$
Summer/fall	−14.5	7.8×10^{-3}	952	32 ± 6	$5.10 \times 10^{-3} \pm 5\%$

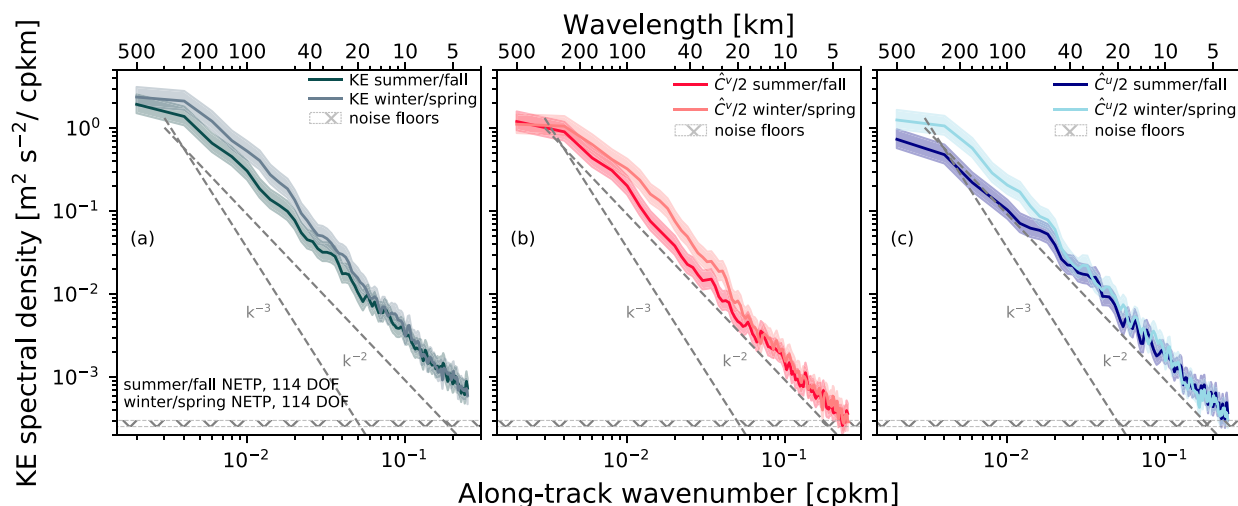


FIG. 4. Seasonal kinetic energy (KE) spectra for ADCP data in the northeast tropical Pacific NETP. Light colors denote winter/spring means, while darker colors denote the summer/fall means. (a) Total KE, (b) cross-track component, and (c) along-track component. The hashed area in (a)–(c) is the interval between the noise floor estimated in winter/spring and the noise floor in summer/fall. Noise is typically higher in winter.

IGW seasonality in the DTNEP and SETP, where we see sufficiently strong restratification to support increased IGW amplitude in summer/fall.

In terms of the mixed layer, in the DTNEP the mixed layer depth cycle is weaker than in the other regions, and summer/fall mixed layers in this area are expected to be shallower than 30 m, while elsewhere the mixed layer is always deeper than 30 m (Table 2). The NETP and SETP see a large cycle in mixed layer depth (Table 2). The deep (>50 m) winter/spring mixed layers in the two regions would favor the onset of mixed layer baroclinic instabilities (Boccaletti et al. 2007), which potentially energize the balanced spectra (Callies et al. 2016) and small-scale divergence (e.g., Cao et al. 2021). This is consistent with the vortex results for the NETP but not for the SETP. For instance, recalculation of NETP spectra using ADCP data from April or May, when averaged mixed layers are shallower (instead of November or December), suppresses the seasonality somewhat through a decrease in the vortex KE.

In contrast, we do not expect background EKE to drive seasonality in the vortex spectra. Seasonal differences in EKE are small, and regional differences are more noteworthy. Background EKE is largest in the DTNEP, where it is roughly twice that of the NETP and 5 times stronger than in the SETP (Table 2). Background EKE in the NETP and SETP peaks around July and is weakest in December–January; in the DTNEP, the EKE seasonal cycle is less defined. The cycles' amplitudes are close to the uncertainty (Table 2).

4. How robust are the estimates?

a. Are assumptions satisfied?

To assess the fidelity of the results, we evaluated the assumptions underlying the Helmholtz decomposition for 1D data. Bühler et al. (2017) listed statistical metrics for 1D current

observations to diagnose the presence of anisotropy and serial correlation between rotational and divergent fields. One metric for anisotropy is the expected value of the difference between variance in the along-track component and variance in the cross-track component (i.e., $\mathbb{E}[u^2 - v^2]$). A second metric is significant correlations between u and v , i.e., $|\mathbb{E}[uv]| \neq 0$, or more usefully the cross-spectrum between u and v (see also supplement text). Isotropic rotational and divergent fields will lead to zero cospectra and quadrature spectra. A significant quadrature spectrum indicates that the two fields are correlated (Bühler et al. 2017).

These quantities, computed for example subsets of the ADCP data in Fig. 6 (also in Fig. S4 for the other regions), indicate that the assumptions of isotropy and uncorrelated rotational and divergent components are sufficiently satisfied. This is demonstrated by the fact 1) that we either find small values for both $\mathbb{E}[u^2 - v^2]$ and $\mathbb{E}[uv]$ [$O(1\%)$ of the variance] or we find $\mathbb{E}[uv] \ll \mathbb{E}[u^2 - v^2]$ when $\mathbb{E}[u^2 - v^2]$ is $O(10\%)$ of the variance (Figs. 6c,d), and 2) that there is a lack of a significant coherent cross-spectra between the along- and cross-track velocities (in either the imaginary or real components; Figs. 6a,b). For context, in the anisotropic Gulf Stream region, Bühler et al. (2017) found $\mathbb{E}[uv]$ to be 20% of the variance and the ratio of $\mathbb{E}[uv]$ to $\mathbb{E}[u^2 - v^2]$ to be close to 1. In contrast, we find ratios closer to 0.1. These results are insensitive to the amount of data (cf. the blue colors and filled lines for collocated data to the orange and dashed lines for all data in Fig. 6) or to any particular choice of data aggregation (Figs. S3d–f).

Small, nonzero values of $\mathbb{E}[u^2 - v^2]$ and $\mathbb{E}[uv]$ can arise in at least two other ways: biased sampling and nonwhite measurement noise (see the appendix). The latter may be relevant to understand the presence of weak cross-spectral energy (e.g., Figs. 6a,b) and small . The former provides an explanation for the larger $\mathbb{E}[u^2 - v^2]$ relative to $\mathbb{E}[uv]$ (e.g., Figs. 6c,d; i.e., the low ratio mentioned above): a negative $\mathbb{E}[u^2 - v^2]$ can arise in a rotation-dominated isotropic field or in an

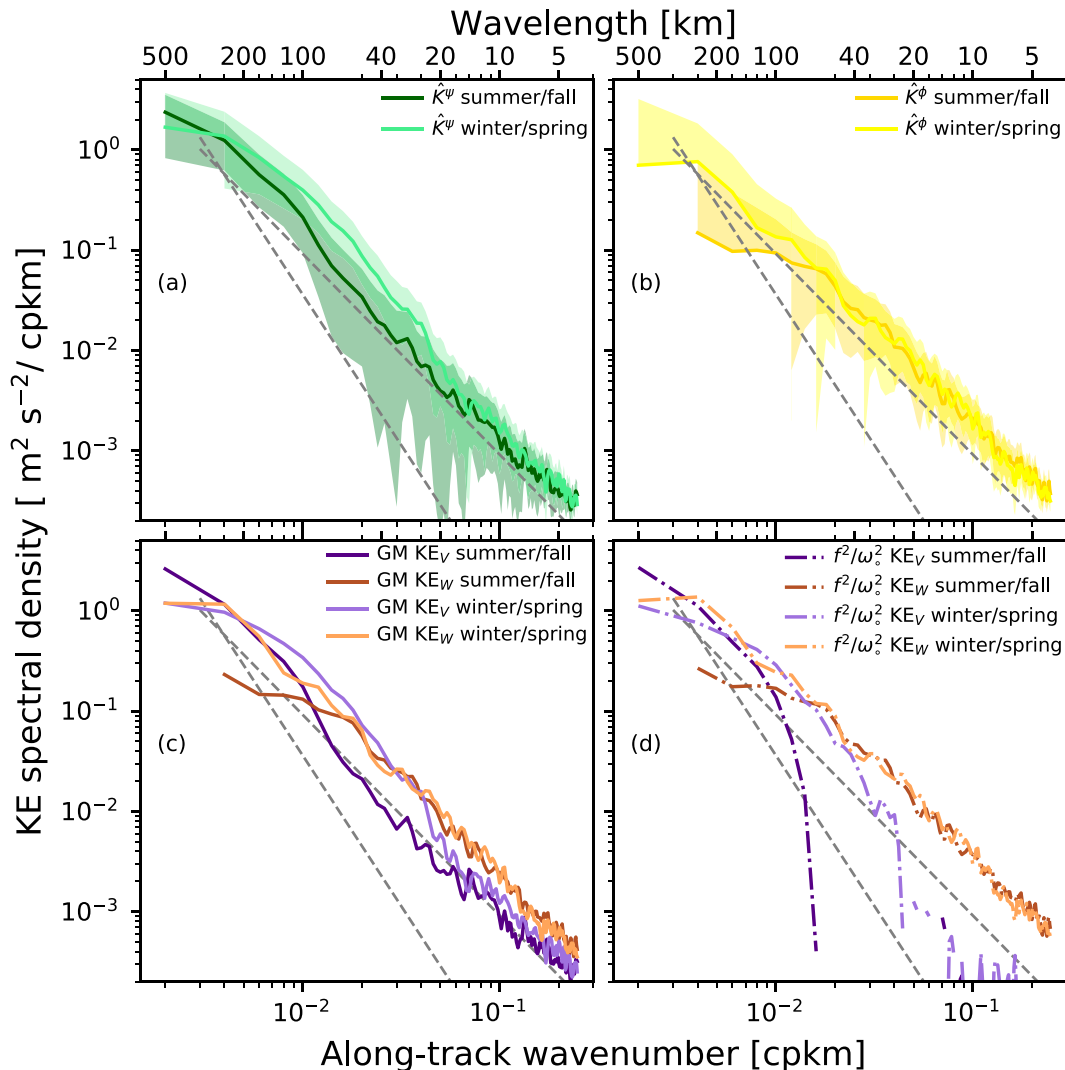


FIG. 5. Helmholtz and wave-vortex decompositions of the seasonal kinetic energy (KE) spectra for ADCP data in the northeast tropical Pacific NETP. Light colors denote winter/spring means, while darker colors denote the summer/fall means. (a) The rotational component, (b) the divergent component, (c) the wave-vortex decomposition using the Garrett-Munk spectrum, and (d) the decomposition using the constant f^2/ω_*^2 .

anisotropic field that is preferentially sampled parallel to anisotropy in the rotational or sampled perpendicular to anisotropy in the divergent field. While conceivable, the anisotropic case is arguably less likely than the isotropic case; furthermore, we found no sensitivity to sampling direction (Fig. S12).

b. Significance tests through randomized resampling experiments

We detect seasonality in the NETP KE spectra and power ratio (Figs. 4a–c): seasonal differences, though not particularly strong, exceed 95% uncertainty levels. We use randomized resampling experiments to more formally test whether these seasonal differences in power ratio, slope, and anisotropy metrics are likely to arise by chance sampling. For the NETP seasonality experiment, 60 samples were randomly drawn without repetition from the combined summer/fall and winter/spring

data pool to create two groups. We perform 10 000 realizations and record the differences in the above parameters between the two groups. We plot the differences in power ratio that were frequently recorded (the 33rd and 66th percentiles, dotted lines in Fig. 7a), and those rarely recorded (the 2.5th and 97.5th percentiles, dashed lines in Fig. 7a). The observed power ratio (blue line in Fig. 7a) lies mostly within the less-likely range, especially for the largest scales and for the ~25–50-km band, showing that the seasonal difference is unlikely to be a statistical fluke.

The differences between seasons in slope, $\mathbb{E}[u^2 - v^2]$, $\mathbb{E}[uv]$ (cf. Fig. 6c versus Fig. 6d and dashed lines in Fig. 7b) could be a chance outcome (they do not exceed the 95% likelihood, Fig. 7b). The same resampling experiment applied to the DTNEP and SETP indicates that the small seasonal differences could arise from chance sampling. The resampling experiments also show that the uncertainty due to sampling in area-mean

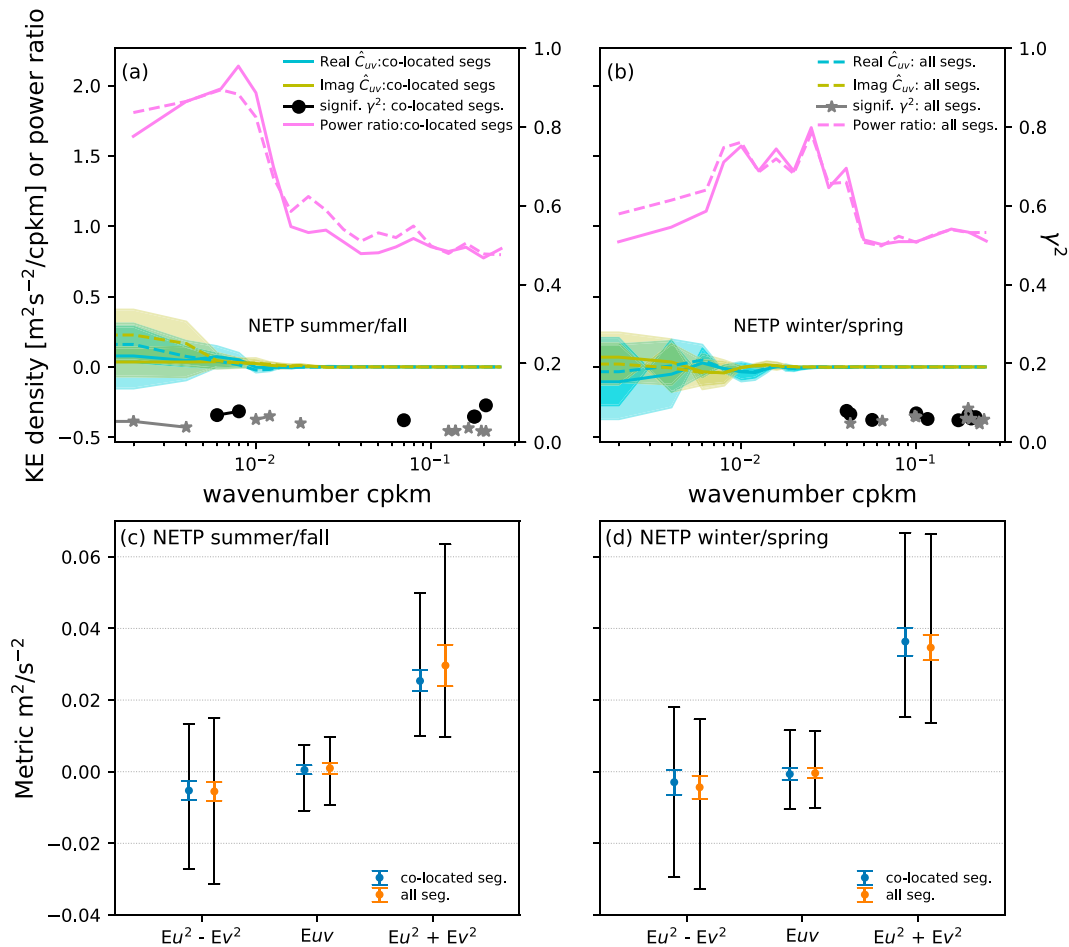


FIG. 6. The cross-spectra (real and imaginary components) and spectral coherence squared (γ^2 , right y axis) for collocated segments (i.e., consistent geographical coverage; solid lines, circles) and for all available segments (dashed lines, stars) in the northeast tropical Pacific (NETP) domain during (a) summer/fall and (b) winter/spring; the magenta lines are the mean cross- to along-track power ratios. Shading gives the 95% confidence interval, and we only show coherences that are significant at the 95% level. (c),(d) $\mathbb{E}[u^2 - v^2]$, $\mathbb{E}[uv]$, and $\mathbb{E}[u^2 + v^2]$ (variance) for summer/fall and winter/spring in the NETP, respectively; the blue bars consider only transect segments that are collocated, orange all segments available within the region/season; the colored bars show twice the standard error of the mean and the black bars show the 5%–95% range.

spectral properties, in all cases, is significantly smaller than the χ^2 based uncertainty (Figs. S3a–c), and we do not find significant differences between any two random subsets, including for the diagnostic metrics (Figs. S3d–f). This result suggests fairly homogeneous statistics within the three domains, as further implied by the statistically insignificant differences between choice subregions within the domains.

5. Consistency with 1D decompositions of model fields

To place the observations in context, we carry out equivalent analyses using output from the LLC4320 model, both along latitude/longitude grid lines and along ship tracks. The model produces annual- and domain-mean KE spectra with slopes near -2 for the 20–200-km wavelength interval, similar in that sense to the ADCP results, albeit less energetic at low wavenumbers (Figs. 8a–c) and with a prominent energy decay

at high wavenumbers, which combine to confer a curvier aspect to the model spectra. Power ratios and Helmholtz and wave–vortex decompositions are consistent with dominantly divergent, IGW motions (Figs. 8d–i), as seen in the ADCP and in the Qiu et al. (2018) analysis. The most obvious differences between model and ADCP results are that model spectra display much higher ratios of divergent-to-rotational energy, and hence also higher ratios of wave-to-vortex energy, as demonstrated by the model’s high ratio of along-track to cross-track power at submesoscales, particularly for the DTNEP and the SETP (Figs. 8e,h,f,i). In the NETP, the levels of divergence in the model show better agreement with ADCP but are still high. The results are fairly insensitive to sampling strategy (cf. calculations using zonal lines, shown by the dashed lines, versus those from ship tracks shown by solid lines in Fig. 8).

Qualitatively, the model annual-mean transition scales, as estimated with the 1D method, capture the regional pattern

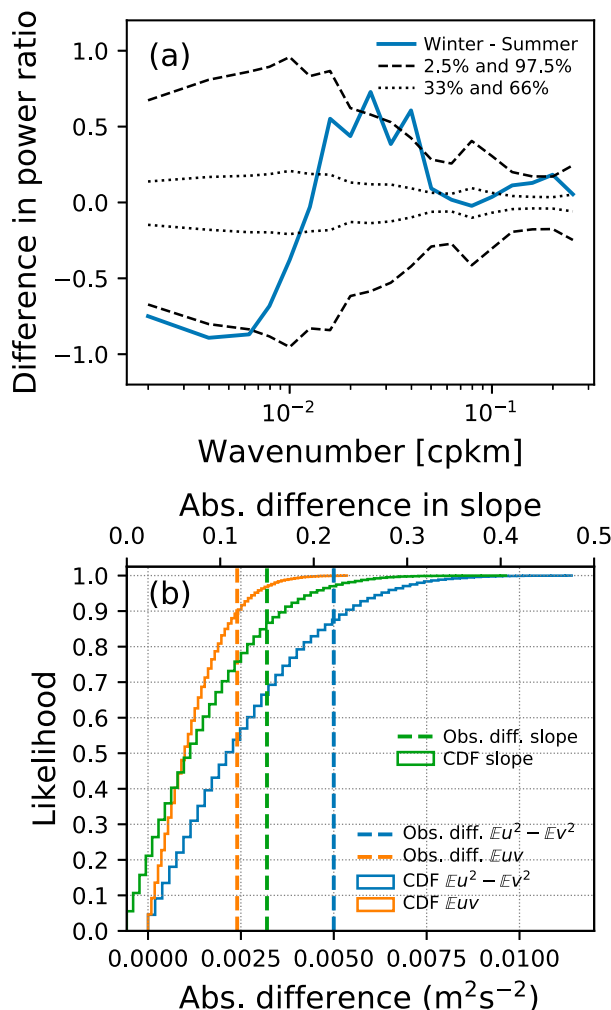


FIG. 7. (a) The difference in power ratio between winter/spring and summer/fall averages (blue; data have been averaged by decade) in the northeast tropical Pacific vs the 33rd and 66th percentiles (dotted black lines) and 5th and 95th percentiles (dashed black lines) of the differences between two random subsets from the resampling experiment, using data from both seasons. (b) Cumulative distribution functions for the differences in $\mathbb{E}[u^2 - v^2]$ (blue) and $\mathbb{E}[uv]$ (orange) and slope fit (green); the color-matched dashed lines show the observed value of the difference in the parameters.

seen in the observations (Table 1). Quantitatively, the model transition scale agrees well with the ADCP scale in the SETP (Table 1), but not in the DTNEP, where model scales are much longer despite significant divergence overestimation in both regions (in the DTNEP, the model also shows a lack of vortex KE). For the NETP, the transition scale is also longer than observed (Table 1), despite a much smaller overestimation of divergence when compared to the other regions.

Unlike the ADCP, in the model all regions show low ratios of \hat{C}_ψ^u to \hat{C}_ϕ^v (Figs. 9a–c), particularly during summer/fall. The ratios are often below the predictions by the GM spectral model, with values approaching those associated with the M_2 internal tide (gray dashed lines in Figs. 9a–c), particularly in

the DTNEP (Fig. 9b). An intense internal tide in the model would explain the excess divergence. The exception is the NETP during winter where ratios are ≥ 1 (Fig. 9a), suggesting a departure from an IGW dominated scenario.

The model captures the observed seasonal patterns, or the lack thereof (in the case of the DTNEP and SETP) reasonably well (e.g., Fig. 10 versus Figs. 4a and 5c). We recover large seasonality in the NETP transition scale (Table 1), which is driven by intense winter forcing of the vortical/rotational component (Fig. 10b). This enhancement is about 50% stronger than observed (Fig. 5c). The summer/fall vortex KE is much weaker than observed, however. Combined with the overestimated divergent/IGW field, this partially explains the mismatch of scales in the NETP.

An important question is how methodology affects the model–ADCP differences. Within the model, we assessed the impact of geographical sparseness, direction of sampling, and accuracy of the Helmholtz decomposition. Figures 8b, 8c, 8e, and 8f show differences in power ratios and Helmholtz decompositions between zonal and ship-sampled spectra. The ship tracks sample preferentially in the north–south direction. (Meridional spectra are not shown because they are very similar to “ship” spectra.) In our evaluations of the accuracy of the Helmholtz decomposition [by comparing against spectra of \hat{K}^ψ and \hat{K}^ϕ obtained from a full, 2D Helmholtz decomposition of model currents using the Smith (2008) algorithm], the meridional or ship component is generally less accurate than the zonal component (typical accuracy 30% versus 10%, respectively, Figs. 9d–f, also note the biases). The cause of this lower accuracy is the combination of anisotropy in the 2D spectra of ψ and/or ϕ , prominent in several locations, e.g., the DTNEP, with a strong dominance of one of the components.

As cautioned earlier, the transition scale, as inferred from the crossover scale, is imprecise; it is sensitive to relatively small errors in the decomposition (e.g., Figs. 9d–f) and/or uncertainty in the spectrum (e.g., Fig. 4), especially at low wavenumbers, even from model output (e.g., Fig. 8). Transition scales longer than 250 km are quoted here for intercomparison purposes and are not to be taken literally. Propagating a 25% error in the Helmholtz decomposition cannot account for the wide difference between model and ADCP. The limitations of the 1D method thus do not alone explain the transition scale differences, unless there are additional and substantial failures of the wave–vortex assumptions; this is discussed further below.

The sampling experiments show that the ship sampling is sufficient to provide robust spectral estimates. Since differences between sampling configurations are negligible, in the remainder of this paper we show only results from the realistic sampling configuration in Figs. 8–10.

6. Discussion

a. Comparison with previous studies: How different is the SETP/NETP from other regions?

1) ADCP KE SPECTRA

It is instructive to compare our results with those of similar studies. When compared to Gulf Stream, Drake Passage, and Kuroshio spectra (e.g., Callies and Ferrari 2013; Rocha et al.

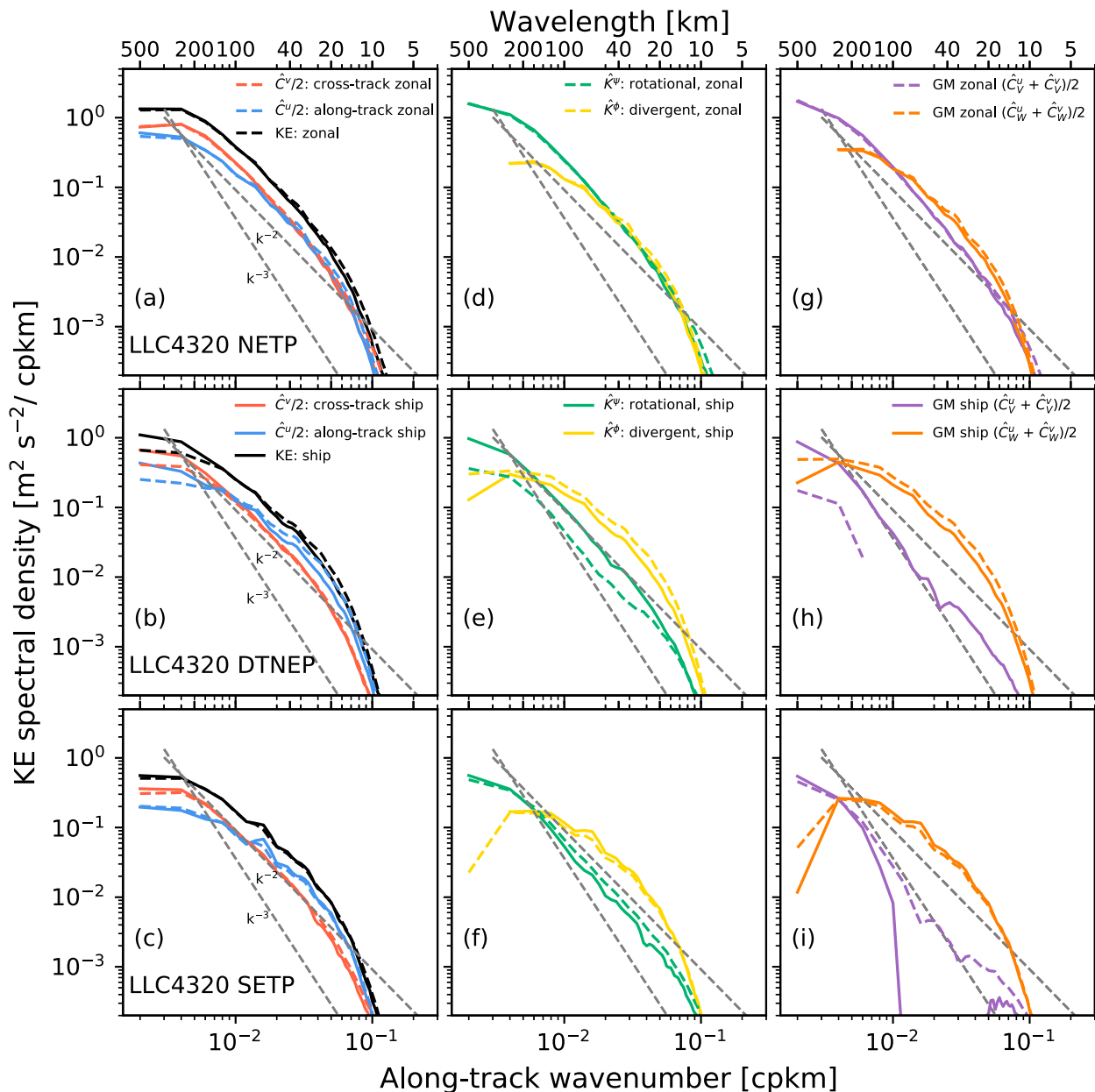


FIG. 8. As in Fig. 2, but for the LLC4320 model surface output. The annual-mean spectral averages shown here are calculated from (dashed lines) weekly output taken along zonal grid lines, and from (solid lines) output interpolated onto the ship tracks of the corresponding month (realistic sampling experiment, see main text for definition). The large number of samples practically reduces statistical uncertainty to zero. For the wave–vortex decomposition we use the Garrett–Munk spectrum with parameters from Table 2.

2016a; Qiu et al. 2017), eastern tropical Pacific spectra are weaker at the larger scales and much flatter for 20–200 km scales. The KE spectra in the SETP and DTNEP (Figs. 2b,c) have energy levels and slopes that are similar to values found in the spectrum from the North Equatorial Current (NEC) in the western Pacific (Qiu et al. 2017), with the caveat that while we focus solely on the near surface 30-m bins, Qiu et al. (2017) analyze vertically averaged velocities between 40 and 100 m. The ratios of divergent and IGW energy to rotational and vortex energy, respectively, are much larger

here than anywhere else, despite being surface-only estimates, where one would expect a larger vortex-to-IGW ratio. The KE spectrum in the NETP (Figs. 2a,d,g) is similar to that of the California Current (Chereskin et al. 2019); it is also roughly similar to the one Qiu et al. (2017) found for the subtropical countercurrent region of the western Pacific (which encompasses the latitudinal range used here), although the energy level is noticeably weaker in the NETP, mostly because of weaker rotational/vortical components; both regions show similar seasonal patterns.

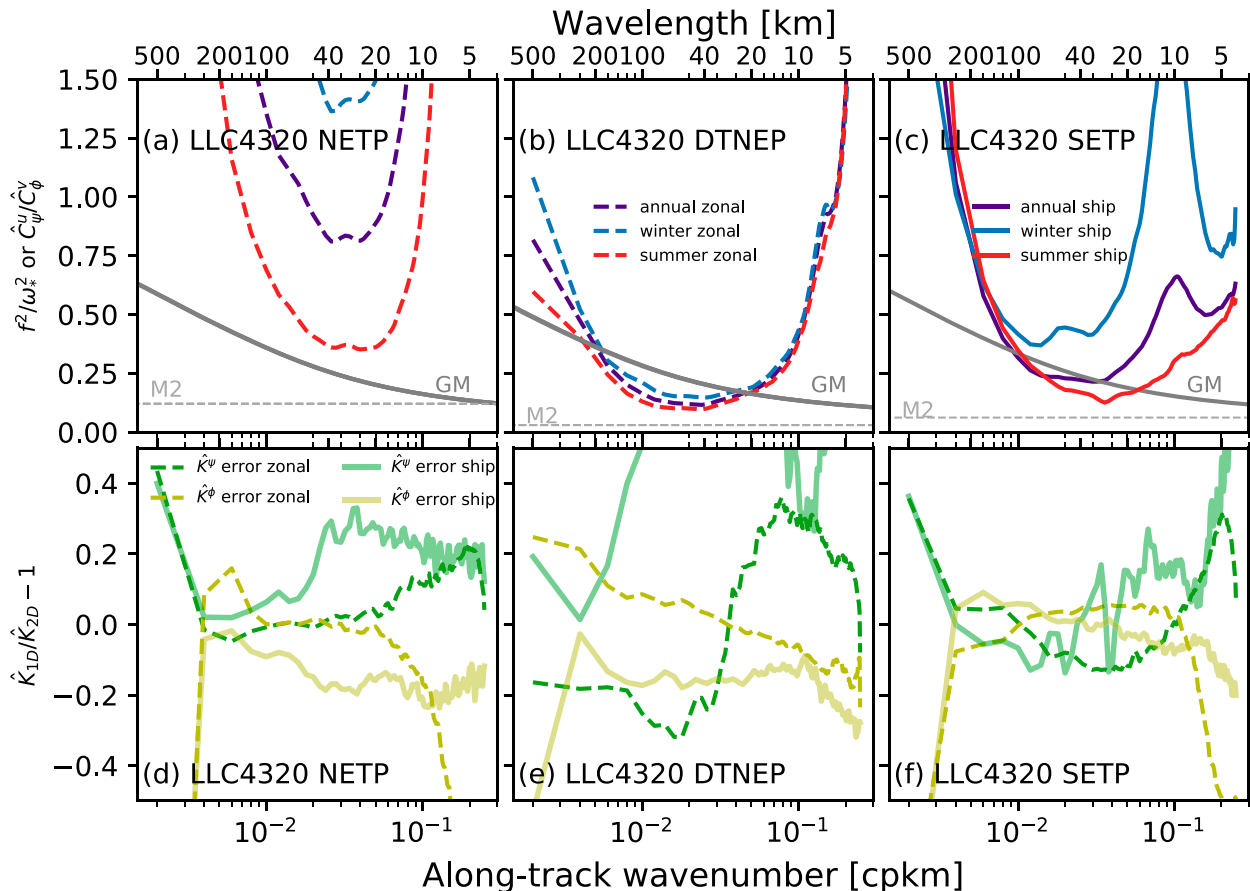


FIG. 9. (a)–(c) The ratio of \hat{C}_ψ^u to \hat{C}_ψ^v , equivalent to f^2/ω_*^2 , derived from the 1D Helmholtz decomposition of LLC4320 model surface currents; curves are color-coded by season, and we also show Garrett–Munk and M_2 internal tide predictions for f^2/ω_*^2 in gray. (d)–(f) Error of the 1D Helmholtz decomposition for annual-mean spectra; the error is defined as the difference between the 1D spectral decomposition and the spectra from a 2D Helmholtz decomposition using the method of Smith (2008) based on properties of Fourier transforms, which makes it well suited for spectra. In all panels, dashed lines are for samples along zonal model grid lines; solid lines are for calculations with ship sampling of model output, which is the preferred ratio comparison method when it is as accurate as other sampling schemes.

2) TRANSITION SCALE LONGER/SHORTER THAN WHAT QIU ET AL. (2018) FOUND?

Our study set out to provide observation-based estimates of the transition scale to complement model-derived efforts, so here we compare ADCP and LLC4320 results. Uncertainty notwithstanding, ADCP data show longer transition scales in the NETP than the model analysis of Qiu et al. (2018) (Table 1); in the DTNEP, ADCP data show a shorter transition scale, while the agreement is better for the SETP. Qualitatively, the observational regional and seasonal patterns (or lack thereof) compare well with the Qiu et al. (2018) results. As discussed in section 5, we do not expect these model–ADCP differences in transition scale to be driven by the 1D techniques. We determined that differences between the model results reported here and in Qiu et al. (2018, obtained using frequency–wavenumber spectra), as summarized in Table 1, result primarily from area-averaging the KE spectra before determining the transition scale, and only secondarily from the 1D wave–vortex decomposition assumptions, mostly

the use of the GM spectrum rather than the exact model IGW climate.

3) MODEL REALISM

While model and ADCP may have qualitatively similar transition scales, our analysis reveals substantial differences in the KE spectra and their decomposition: relative to observations, the LLC4320 has weaker large-scale KE (e.g., Figs. 8a–c versus Figs. 3a–c), more divergence at submesoscales everywhere in the eastern tropical Pacific, and stronger seasonality in the NETP. We contend that the differences result in large part from the model’s forcing fields and parameters. The LLC4320 simulation used overly strong tidal forcing (Mazloff et al. 2020) and has weak near-inertial forcing (Yu et al. 2019; Arbic et al. 2022). This combination could explain the low f^2/ω_*^2 ratios we detected in the model using the Bühler et al. (2014) method. We do not have an explanation for the model’s weaker background EKE or the stronger balanced seasonality. Interannual variations are unlikely to be a key factor

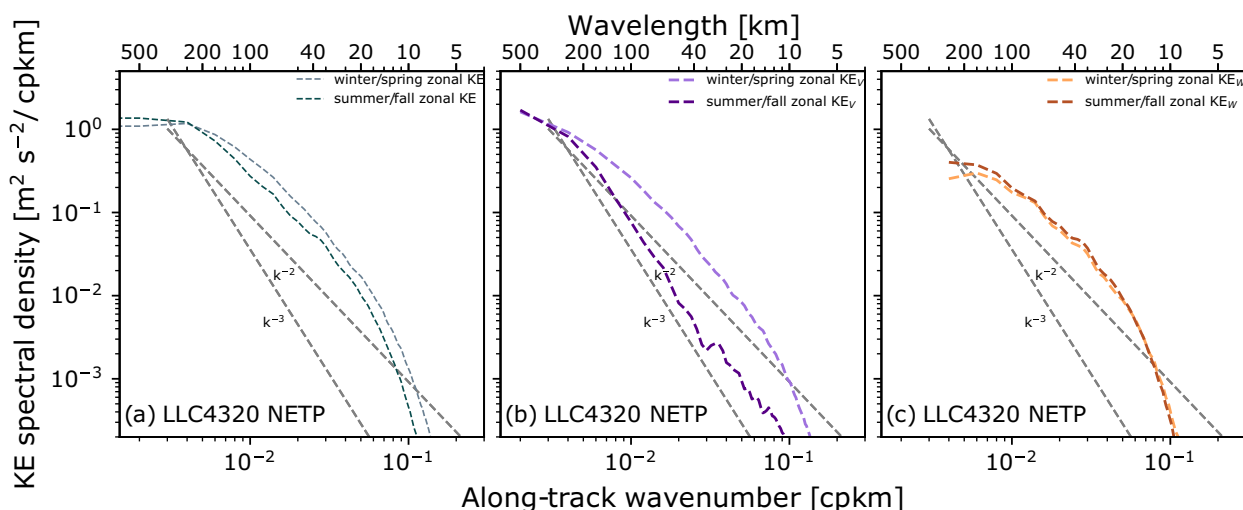


FIG. 10. Surface kinetic energy (a) spectra and their (b) vortex and (c) wave components for winter/spring (light colors) and for summer/fall (dark colors) in the northeast tropical Pacific NETP using the LLC4320 model. The spectral averages shown here are calculated (dashed lines) along zonal grid lines since they are nearly equal to those calculated along ship tracks. For the wave–vortex decomposition we use the Garrett–Munk spectrum with parameters from Table 2. The other regions that lack seasonality are in Fig. S8.

accounting for these differences, as we find no evidence of significantly anomalous mixed layers or EKE during 2011/12 (Table S2).

4) ADCP VORTICAL DYNAMICS: SPECTRAL SLOPES AND THEORIES

The slope of the geostrophic KE spectrum is a useful clue to identify the dominant dynamical regime (e.g., [Callies and Ferrari 2013](#)). In all regions in summer/fall, regardless of whether the IGW field is dominated by near-inertial waves (NIWs) or obeys the GM spectra, the near-surface ADCP vortex spectral slope is closer to -3 than to -2 and thus more consistent with the interior QG prediction, akin to the findings for the Drake Passage ([Rocha et al. 2016a](#)) and the Gulf Stream ([Bühler et al. 2014](#)). In the SETP, there is no evidence for seasonality in the vortex slope, and slopes are closer to -3 than -2 year-round, regardless of which IGW model is used in the decomposition. In winter/spring in the northern tropics, the situation is ambiguous. In the NETP, the vortex slope is near -2 , a characteristic associated with theories of mesoscale-strain-driven frontogenesis and/or mixed layer instabilities (e.g., [Callies et al. 2016](#)). In the DTNEP, the vortex component is much weaker than the IGW component, and its slope depends strongly on the IGW model choice; therefore, we do not deem this flattening to be robust enough to indicate a regime change.

5) WHAT DYNAMICS BEST EXPLAIN THE OBSERVED SEASONAL AND REGIONAL TRANSITION SCALE PATTERNS?

[Qiu et al. \(2017\)](#) argue that the transition scale is inversely proportional to background mesoscale EKE, which would control the submesoscale spectrum. We see no evidence that this occurs here: the region with the most background EKE that we examined (DTNEP) shows the longest transition

scale, and background EKE seasonality is weak and often out of phase with submesoscale KE. The winter KE increase due to the vortex component, spectral slope near -2 , and transition scale decrease suggest that submesoscale vortical dynamics in the NETP are driven by mixed layer instability rather than mesoscale strain. For observed winter/spring mixed layers, stratification and mean vertical shears in the NETP, the mixed layer instability injection wavelength ([Boccaletti et al. 2007](#); [Nakamura 1988](#)) is ~ 30 km. Enhancement of balanced KE at larger scales would follow from the establishment of an inverse cascade ([Callies et al. 2016](#)). Previous evidence for a winter increase in KE consistent with mixed layer instabilities was confined to the subtropics ([Callies et al. 2015](#); [Buckingham et al. 2016](#)). The transition scale in the DTNEP and SETP would be controlled by the IGWs. From moored data, [Boyer and Alford \(2021\)](#) find an energetic IGW continuum ($\sim 5 \times$ canonical GM) in the Southern Hemisphere tropics, as well as energetic internal tide and NIW components; this is consistent with the SETP ADCP showing lower f^2/ω_s^2 than the other areas and provides additional evidence for a generally energetic IGW field there. In the DTNEP, the lack of observations hinders a similar conclusion. We also do not find a discernible fingerprint of tropical instability waves in the DTNEP from our results, likely because they are mostly active south of our boundary (e.g., [Wang et al. 2018](#)).

b. Caveats

1) ALIASING BY TIDAL AND INERTIAL OSCILLATIONS OR OTHER VIOLATIONS OF FAST TOW

Low-mode internal tides and NIWs are of concern for two reasons: they violate the fast-tow assumption, and they are highly anisotropic motions. The questions are how these special IGW classes distort expected cross- and along-track power ratios and how likely it is that the Doppler shift spreads

energy at discrete wavenumbers across multiple wavenumbers. If k and ω are the true along-track wavenumber and frequency of a feature, and U is the ship's velocity component in the along-track direction, then the estimated wavenumber is $\hat{k} = k(1 - \omega/kU)$. At typical ship speeds ($U \geq 4 \text{ m s}^{-1}$), the fast-tow assumption ($kU \gg \omega$) is adequate for the longer scales dominated by the slowly evolving mesoscale, for sub-mesoscale-range motions with time scales near f (thus especially in the tropics), and for the short scales dominated by the equally slow high vertical mode IGWs (Chereskin et al. 2019). The fast-tow assumption may also be impacted by the presence of hydrographic stations in some of the analyzed 500-km segments (i.e., ship stops lasting under 2 h), particularly in areas of energetic low mode IGWs, but past experience indicates that this is not a concern if the transect-averaged ship speed is much higher than the first baroclinic mode (Chereskin et al. 2019).

Wind-generated NIWs initially have scales of several hundreds of kilometers; the β effect is effective at generating shorter scales, decorrelating the surface motions, and, via pumping, inducing downward and equatorward radiation (e.g., D'Asaro 1989). While NIWs are a broadband phenomenon, only the longest wavelengths have phase speeds comparable to that of low modes, which are close but slower than typical ship speeds. We carried out synthetic experiments to examine the effect of ship sampling of monochromatic NIWs on the observed power ratio and \hat{k} . At typical ship speeds, in the tropics, we find that an initially homogeneous ($k = 0$) mixed layer inertial oscillation, whether sampled zonally or meridionally, projects onto scales much longer than $\sim 300 \text{ km}$, with power ratio 1 (the true ratio) only if phases are adequately averaged. In this case we also expect dominant anticyclonic rotation with time and thus also along the direction of sampling. This pattern holds for wavelengths equal to and longer than $\sim 300 \text{ km}$ and indicates that a single long NIW event can masquerade as either a purely rotational or a purely divergent large-scale motion. A few transects taken during winter months show high large-scale along-track power and predominantly clockwise rotation, affecting some ensemble averages (e.g., Figs. 4c for the first and Fig. S5b for the second). They could result from the sampling of a particular event of long NIWs and help explain the small power ratios in Fig. 6b and large wave KE in Figs. 5c and 5d at long scales. As NIW scales decrease below 300 km , the power ratio becomes much less sensitive to ship sampling and $\hat{k} \rightarrow k$. There is also no longer a preferred rotation sense, which is consistent with the ADCP rotary spectra (Fig. S5).

The mode-1 internal tide has a phase speed of $\sim 3 \text{ m s}^{-1}$, close to but still less than typical ship speeds. The SETP has relatively strong M_2 internal tides (see SSH amplitude maps in Ray and Zaron 2015; Zhao 2017), with a $O(100) \text{ km}$ wavelength for mode 1 (less for the slower higher modes). In principle, ship sampling smears the internal tide peaks in wavenumber space (the expected wavelength range is $200\text{--}90 \text{ km}$ for mode 1). This could explain why the ADCP data do not show an internal tide peak in contrast with altimeter observations (e.g., Ray and Zaron 2015). Because the internal tide here propagates meridionally, and most

ship tracks are oriented meridionally, we would expect the aliased energy to project onto the along-track component, leading to an overestimate of the divergent/IGW KE in these bands. Internal tide peaks, however, are absent from the instantaneous model samples, whether taken along ship tracks or on zonal grid lines. We therefore do not expect a large smearing effect in the observations. This key assumption deserves to be examined systematically in future studies.

2) ASSUMPTIONS FOR THE 1D HELMHOLTZ AND WAVE-VORTEX DECOMPOSITION

The decompositions presented here rely on the assumptions that the velocity statistics are stationary, homogeneous, and isotropic. While we were able to evaluate the last two, we do not know how well stationarity holds. The overall sparseness of the cruise data prevents adequate binning to unambiguously assess the role of interannual variability, which is seen in the two key environmental drivers of the KE spectra: mixed layer depth and background EKE.

Another important assumption is that all divergence is due to IGWs. Further model analysis by Torres et al. (2018) supports use of this assumption for the low EKE regions that we examine here, yet during winter, the model shows nonnegligible ($\sim 30\%$) contributions from nonwave motions at high wavenumbers in some areas (Figs. 11a,b in Torres et al. 2018, or Fig. S9). It is not obvious that these are also the case for the observations; since the spectra of divergence have no seasonality, attribution of the divergent energy to a specific process is ambiguous. To circumvent this issue, we take the opposite approach: we assume that all ADCP rotational energy is due to eddy motions and estimate the Rossby number as $R_o = \sqrt{k^3 \hat{K}^{\psi}}/f$ (Callies et al. 2015). The R_o at submesoscales (Fig. 11) are at most $O(0.1)$, so unlikely to support significant divergence, implying the original assumption holds. Divergent corrections to the vortical KE, however small they may be, would still be useful to explore, as this assumption impacts the accuracy of the result that KE within the submesoscale transition range (Figs. 3d–f) appears to be composed of NIWs.

The appropriateness of an IGW spectral model is difficult to evaluate independently. Our results agree with those of Chereskin et al. (2019) in showing rather limited agreement with the GM model. This could be a near-surface effect; GM behavior could occur deeper in the water column, but ADCP signal-to-noise issues prevent more in-depth analysis at present. Analysis of deeper layers are thus left for a future study.

This surface behavior is unlikely to be caused by wave refraction processes and could reflect NIW sources. The L02 framework indicated little impact of the mixed layer in near-surface values of the wave rotation to divergence ratio. While the Bühler et al. (2014) IGW energy equipartition statement is not formally valid in the abrupt transition between the mixed layer and the thermocline, we estimate, using the L02 framework, that the resulting error of the WKB approximation breakdown is smaller than the uncertainties reported so far. Details of these analyses are in the supplement. Finally, as the mixed layer depth varies along transects, the ADCP 30-m bin

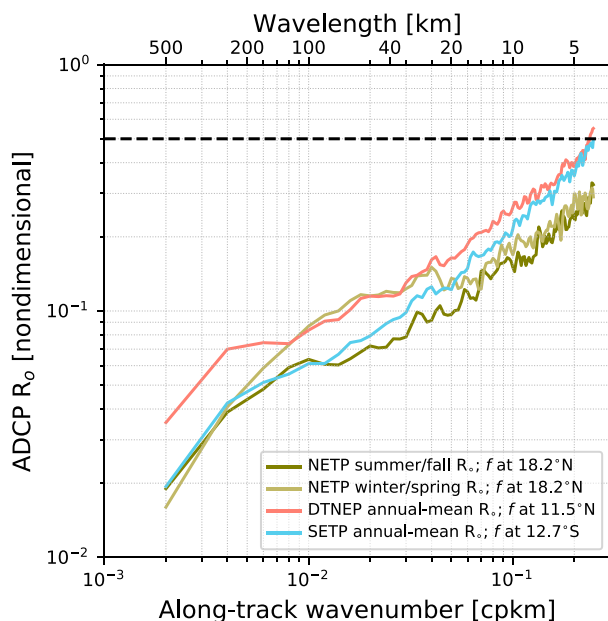


FIG. 11. Rossby number R_o estimated from the rotational component of ADCP data in the three domains in the east tropical Pacific. The dashed black line marks $R_o = 0.5$.

averages together mixed layer and thermocline velocities. We cannot therefore rule out that a mixture of IGW and nonwave or mixed layer-only processes contributes to the high rotation to divergence ratio.

c. Implications for high resolution and swath satellite altimetry

In the eastern tropical Pacific, the fact that a large portion of the variability of near-surface currents is divergent, potentially IGW driven, reduces the range of usefulness of altimetric derived current data. Our estimates of the transition scale suggest that we should expect dominant geostrophic currents for scales longer than about 200 km over most of this area, potentially for scales as short as 50 km during certain seasons and limited areas (e.g., NETP). The usefulness of the transition scale to interpret any given or a few submesoscale-permitting altimeter passes/swaths is limited by our inability to constrain the stationarity assumption. Nonetheless, for those interested in the absolute transition scales, we note that there are no obvious reasons to doubt their estimated ranges. Accessing the balanced KE at wavelengths near or immediately below the transition scale will depend not only on the altimeter's true signal-to-noise ratio, but also on the frequency content of the IGWs. Neither is currently well known. If NIWs indeed dominate the near-surface unbalanced wavenumber spectrum, their weak projection onto SSH (Gill 1982) would not hinder detection of the balanced component. Since an analysis by Callies and Wu (2019) further suggests that the IGW continuum lies below the SWOT noise floor, this part of the IGW spectrum would also not hinder the balanced component detection in the tropical eastern Pacific. In contrast, extracting the balanced component from a spectrum with

strong incoherent internal tides, as in the LLC4320 output (Arbic et al. 2022), would be more challenging.

7. Conclusions

In this study we have computed KE spectra from 30-m depth currents measured by underway shipboard ADCPs in the eastern tropical Pacific. The spectra were partitioned into rotational and divergent components and subsequently into wave and vortex parts using the method of Bühler et al. (2014). Our main conclusions are as follows:

- 1) Divergent motions (Figs. 2d–f), presumably inertia–gravity waves (IGWs), make significant contributions to variability at 100–200-km scales and sometimes dominate the variability at scales below 100 km. The divergent motions are largely responsible for the relative flatness of the KE spectra in the eastern tropical Pacific when compared to other regimes.
- 2) The transition scale (Table 1) at which variability ceases to be predominantly geostrophic varies geographically in the eastern tropical Pacific. It is long in the southeast and deep tropics (≥ 200 km) and relatively short in the northeast tropics (~ 70 km). In the northeast tropics, the scale varies seasonally and increases to ~ 100 km in summer/fall months.
- 3) The inferred IGW field exhibits a rotational-to-divergent ratio (Figs. 3d–f) characteristic of predominantly near-inertial motions. Use of a near-inertial IGW spectrum for the decomposition yields vortical KE spectra in the tropics consistent with interior quasigeostrophic predictions. Deviations of this ratio from that expected from the Garrett–Munk spectrum may also indicate that other unbalanced submesoscale activity, e.g., fronts or instabilities, coexists with IGWs.
- 4) Increased vortical KE during winter/spring in the northeast tropical Pacific (Fig. 5) suggests the importance of mixed layer instabilities. Elsewhere seasonality in the KE spectrum appears to be weak and not statistically reliable, so we refrain from discussing seasonal changes in the characteristics of the balanced component in those regions.
- 5) We find little evidence for seasonality of divergent, IGW KE near the surface. This suggests that no single process that is highly dependent on stratification, such as mixed layer instabilities or IGW refraction, dominates the divergent motions.

While our ADCP results agree qualitatively with analyses of a numerical simulation [those here and in Qiu et al. (2018)], they rely on several strong assumptions. Our evaluation of a number of these assumptions shows them to be reasonably satisfied. However, one key assumption deserves further scrutiny: whether the strong divergent spectrum can be largely attributed to IGWs, such that there exists a wavenumber regime dominated by IGWs. Closely tied to this question, the sensitivity of the wave–vortex decomposition to the frequency content of the IGW model also warrants dedicated investigation. Specifically, what types of IGWs dominate the

observable wavenumber spectra of surface KE and SSH, and how best should they be modeled? Investigation of these questions has the potential to resolve long-standing questions on the dominant phenomenology of submesoscales.

The results from this study will serve as a guide for future studies on the submesoscale transition and for interpreting measurements from new high-resolution altimeters including the forthcoming Surface Water and Ocean Topography (SWOT) mission. In this context, our analysis suggests that in the eastern tropical Pacific, a region of low background eddy kinetic energy, “pure” mesoscale frontogenesis-driven 2D turbulence is not a useful framework to model the variability at scales within the submesoscale transition. In situ observations differ sufficiently from the LLC4320 simulation to caution against overinterpreting model output. Our results also imply that, although the usefulness of geostrophically derived currents in this broad region appears limited to scales resolved by the present constellation of altimeters, the new swath measurements will provide an opportunity to learn more about the global characteristics of submesoscale dynamics. This will require development of strategies to identify the signatures of the processes that comprise the unbalanced regime in the SSH measurements. We demonstrate that historical shipboard ADCPs provide useful data for studying the submesoscale transition, and their potential has yet to be fully tapped.

Acknowledgments. We thank B. Qiu and S. Chen for kindly providing their model transition-scale data and the UHDAS team members for excellent processing of ADCP data. The LLC4320 output is available through the ECCO Data Portal (<https://data.nas.nasa.gov/ecco/data.php>), and the xmitgcm software (<https://xmitgcm.readthedocs.io/en/latest/>) was used to read and manipulate the output. The final, cleaned, segmented transect data used for spectral calculations, along with analysis and plotting codes are at https://github.com/ocesauro/transition_EtropPac_ADCP. Software for postprocessing the underway CODAS data is available at <https://github.com/ocesauro/pysadcp>. The subset of underway data used here is available at <https://doi.org/10.6075/J09Z953Q>. This research has been supported by the NASA Ocean Surface Topography Science Team (Award NNX16AH67G) with additional support for STG from the NASA Surface Water and Ocean Topography Science Team (Awards NNX16AH67G and 80NSSC20K1136). We also thank two anonymous reviewers for their comments.

APPENDIX

Velocity Uncertainty Estimation

The ADCP velocity uncertainty is determined from the RMS of the error velocity, defined as the difference in redundant vertical velocities estimated from opposing beam pairs in 4-beam configurations (data from 3-beam configurations were not used here). The RMS error velocity represents the combined ambient and instrumental noise and is used here because it applies to both narrowband and broadband systems. The RMS error velocity is calculated for each

segment and is typically about 2 cm s^{-1} at the 30-m depth bin where beams are relatively close. To account for the error in ship speed estimated from GPS fixes, we assume a position uncertainty of 5 m and a time interval of 5 min (Rocha et al. 2016a). We then regrid, effectively applying 10–15-min averaging. The typical combined uncertainty is thus $\sim 2 \text{ cm s}^{-1}$. The GPS positioning error in velocity given as above is likely overestimated, at least its effect in the currents at scales above the filter length (3 point, 15 min, 6 km) used in the reference layer and ship GPS speed merging. Because the position error is the same for both along- and cross-track components it also likely does not directly influence the methods used here. We do not explicitly account for heading errors, which can yield large cross-track velocity errors (Firing and Hummon 2010). These are typically dealt with in processing by correcting the gyrocompass heading using differential GPS, but a residual random error $O(0.1^\circ)$, which corresponds to 1 cm s^{-1} uncertainty, usually remains. This residual is expected to be mitigated by averaging.

Assuming that the combined error (error velocity + GPS) is white in wavenumber space, we square the RMS velocities and take the mean of all the segments (dashed lines in Fig. 2). The error velocity wavenumber spectrum, however, is not strictly white but pink (e.g., Fig. S1). We hypothesize that this autocorrelation in error velocity may partially explain the observed weak cross-spectral energy between u and v . Other types of errors are not considered here (e.g., known common biases listed in Hummon and Firing 2003). They are assumed to have been dealt with in processing; otherwise, we discard transects that appear problematic or too noisy. Effects of scattering layers, typically not removed from postprocessed data (Hummon and Firing 2003), are not discussed here as they do not influence near-surface returns.

REFERENCES

- Arbic, B. K., and Coauthors, 2022: Frequency dependence and vertical structure of ocean surface kinetic energy from global high-resolution models and surface drifter observations. arXiv, 2202.08877, <https://doi.org/10.48550/arXiv.2202.08877>.
- Bendat, J., and A. Piersol, 2010: *Random Data: Analysis and Measurement Procedures*. 4th ed. Wiley, 604 pp.
- Blumen, W., 1978: Uniform potential vorticity flow: Part II: A model of wave interactions. *J. Atmos. Sci.*, **35**, 784–789, [https://doi.org/10.1175/1520-0469\(1978\)035<0784:UPVFP>2.0.CO;2](https://doi.org/10.1175/1520-0469(1978)035<0784:UPVFP>2.0.CO;2).
- Boccaletti, G., R. Ferrari, and B. Fox-Kemper, 2007: Mixed layer instabilities and restratification. *J. Phys. Oceanogr.*, **37**, 2228–2250, <https://doi.org/10.1175/JPO3101.1>.
- Boyer, A. L., and M. H. Alford, 2021: Variability and sources of the internal wave continuum examined from global moored velocity records. *J. Phys. Oceanogr.*, **51**, 2807–2823, <https://doi.org/10.1175/JPO-D-20-0155.1>.
- Boyer, T. P., and Coauthors, 2019: World Ocean Database 2018. NOAA Atlas NESDIS 87, 207 pp., https://www.ncei.noaa.gov/sites/default/files/2020-04/wod_intro_0.pdf.
- Buckingham, C. E., and Coauthors, 2016: Seasonality of submesoscale flows in the ocean surface boundary layer. *Geophys. Res. Lett.*, **43**, 2118–2126, <https://doi.org/10.1002/2016GL068009>.

- Bühler, O., J. Callies, and R. Ferrari, 2014: Wave–vortex decomposition of one-dimensional ship-track data. *J. Fluid Mech.*, **756**, 1007–1026, <https://doi.org/10.1017/jfm.2014.488>.
- , M. Kuang, and E. G. Tabak, 2017: Anisotropic Helmholtz and wave–vortex decomposition of one-dimensional spectra. *J. Fluid Mech.*, **815**, 361–387, <https://doi.org/10.1017/jfm.2017.57>.
- Callies, J., and R. Ferrari, 2013: Interpreting energy and tracer spectra of upper-ocean turbulence in the submesoscale range (1–200 km). *J. Phys. Oceanogr.*, **43**, 2456–2474, <https://doi.org/10.1175/JPO-D-13-063.1>.
- , and W. Wu, 2019: Some expectations for submesoscale sea surface height variance spectra. *J. Phys. Oceanogr.*, **49**, 2271–2289, <https://doi.org/10.1175/JPO-D-18-0272.1>.
- , R. Ferrari, J. M. Klymak, and J. Gula, 2015: Seasonality in submesoscale turbulence. *Nat. Commun.*, **6**, 6862, <https://doi.org/10.1038/ncomms7862>.
- , G. Flierl, R. Ferrari, and B. Fox-Kemper, 2016: The role of mixed-layer instabilities in submesoscale turbulence. *J. Fluid Mech.*, **788**, 5–41, <https://doi.org/10.1017/jfm.2015.700>.
- Cao, H., B. Fox-Kemper, and Z. Jing, 2021: Submesoscale eddies in the upper ocean of the Kuroshio extension from high-resolution simulation: Energy budget. *J. Phys. Oceanogr.*, **51**, 2181–2201, <https://doi.org/10.1175/JPO-D-20-0267.1>.
- Charney, J. G., 1971: Geostrophic turbulence. *J. Atmos. Sci.*, **28**, 1087–1095, [https://doi.org/10.1175/1520-0469\(1971\)028<1087:GT>2.0.CO;2](https://doi.org/10.1175/1520-0469(1971)028<1087:GT>2.0.CO;2).
- Chereskin, T. K., S. T. Gille, C. B. Rocha, D. Menemenlis, and M. Passaro, 2019: Characterizing the transition from balanced to unbalanced motions in the southern California Current. *J. Geophys. Res. Oceans*, **124**, 2088–2109, <https://doi.org/10.1029/2018JC014583>.
- D’Asaro, E. A., 1989: The decay of wind-forced mixed layer inertial oscillations due to the β effect. *J. Geophys. Res.*, **94**, 2045–2056, <https://doi.org/10.1029/JC094iC02p02045>.
- de Boyer Montégut, C., G. Madec, A. S. Fischer, A. Lazar, and D. Iudicone, 2004: Mixed layer depth over the global ocean: An examination of profile data and a profile-based climatology. *J. Geophys. Res.*, **109**, C12003, <https://doi.org/10.1029/2004JC002378>.
- Firing, E., and J. M. Hummon, 2010: Ship-mounted acoustic Doppler current profilers. The GO-SHIP Repeat Hydrography Manual: A Collection of Expert Reports and Guidelines, E. Hood, C. Sabine, and B. Sloyan, Eds. IOCCP Rep. 14, ICPO Publication Series Number 134, <http://www.go-ship.org/HydroMan.html>.
- Forget, G., J.-M. Campin, P. Heimbach, C. Hill, R. Ponte, and C. Wunsch, 2015: ECCO version 4: An integrated framework for non-linear inverse modeling and global ocean state estimation. *Geosci. Model Dev.*, **8**, 3071–3104, <https://doi.org/10.5194/gmd-8-3071-2015>.
- Fu, L.-L., and C. Uebmann, 2014: On the transition from profile altimeter to swath altimeter for observing global ocean surface topography. *J. Atmos. Oceanic Technol.*, **31**, 560–568, <https://doi.org/10.1175/JTECH-D-13-00109.1>.
- Garrett, C. J. R., and W. H. Munk, 1972: Space-time scales of internal waves. *Geophys. Fluid Dyn.*, **2**, 225–264, <https://doi.org/10.1080/03091927208236082>.
- Gill, A. E., 1982: *Atmosphere–Ocean Dynamics*. Academic Press, 662 pp.
- Hummon, J. M., and E. Firing, 2003: A direct comparison of two RDI shipboard ADCPs: A 75-kHz Ocean Surveyor and a 150-kHz narrow band. *J. Atmos. Oceanic Technol.*, **20**, 872–888, [https://doi.org/10.1175/1520-0426\(2003\)020<0872:ADCOTR>2.0.CO;2](https://doi.org/10.1175/1520-0426(2003)020<0872:ADCOTR>2.0.CO;2).
- Klein, P., and Coauthors, 2019: Ocean-scale interactions from space. *Earth Space Sci.*, **6**, 795–817, <https://doi.org/10.1029/2018EA000492>.
- Levine, M. D., 2002: A modification of the Garrett–Munk internal wave spectrum. *J. Phys. Oceanogr.*, **32**, 3166–3181, [https://doi.org/10.1175/1520-0485\(2002\)032<3166:AMOTGM>2.0.CO;2](https://doi.org/10.1175/1520-0485(2002)032<3166:AMOTGM>2.0.CO;2).
- Lindborg, E., 2007: Horizontal wavenumber spectra of vertical vorticity and horizontal divergence in the upper troposphere and lower stratosphere. *J. Atmos. Sci.*, **64**, 1017–1025, <https://doi.org/10.1175/JAS3864.1>.
- , 2015: A Helmholtz decomposition of structure functions and spectra calculated from aircraft data. *J. Fluid Mech.*, **762**, R4, <https://doi.org/10.1017/jfm.2014.685>.
- Marshall, J., A. Adcroft, C. Hill, L. Perelman, and C. Heisey, 1997: A finite-volume, incompressible Navier Stokes model for studies of the ocean on parallel computers. *J. Geophys. Res.*, **102**, 5753–5766, <https://doi.org/10.1029/96JC02775>.
- Mazloff, M. R., B. Cornuelle, S. T. Gille, and J. Wang, 2020: The importance of remote forcing for regional modeling of internal waves. *J. Geophys. Res. Oceans*, **125**, e2019JC015623, <https://doi.org/10.1029/2019JC015623>.
- Menemenlis, D., J.-M. Campin, P. Heimbach, C. Hill, T. Lee, A. Nguyen, M. Schodlok, and H. Zhang, 2008: ECCO2: High resolution global ocean and sea ice data synthesis. *Mercator Ocean Quarterly Newsletter*, No. 31, Mercator-Ocean, Ramonville-Saint-Agne, France, 13–21.
- Nakamura, N., 1988: Scale selection of baroclinic instability—Effects of stratification and nongeostrophy. *J. Atmos. Sci.*, **45**, 3253–3268, [https://doi.org/10.1175/1520-0469\(1988\)045<3253:SSOBIO>2.0.CO;2](https://doi.org/10.1175/1520-0469(1988)045<3253:SSOBIO>2.0.CO;2).
- Nelson, A. D., B. K. Arbic, D. Menemenlis, W. R. Peltier, M. H. Alford, N. Grisouard, and J. M. Klymak, 2020: Improved internal wave spectral continuum in a regional ocean model. *J. Geophys. Res. Oceans*, **125**, e2019JC015974, <https://doi.org/10.1029/2019JC015974>.
- Percival, D. B., and A. T. Walden, 1993: *Spectral Analysis for Physical Applications*. Cambridge University Press, 612 pp., <https://doi.org/10.1017/CBO9780511622762>.
- Polzin, K. L., and Y. V. Lvov, 2011: Toward regional characterizations of the oceanic internal wavefield. *Rev. Geophys.*, **49**, RG4003, <https://doi.org/10.1029/2010RG000329>.
- Qiu, B., T. Nakano, S. Chen, and P. Klein, 2017: Submesoscale transition from geostrophic flows to internal waves in the northwestern Pacific upper ocean. *Nat. Commun.*, **8**, 14055, <https://doi.org/10.1038/ncomms14055>.
- , S. Chen, P. Klein, J. Wang, H. Torres, L.-L. Fu, and D. Menemenlis, 2018: Seasonality in transition scale from balanced to unbalanced motions in the world ocean. *J. Phys. Oceanogr.*, **48**, 591–605, <https://doi.org/10.1175/JPO-D-17-0169.1>.
- Ray, R. D., and E. D. Zaron, 2015: M_2 internal tides and their observed wavenumber spectra from satellite altimetry. *J. Phys. Oceanogr.*, **46**, 3–22, <https://doi.org/10.1175/JPO-D-15-0065.1>.
- Rocha, C. B., T. K. Chereskin, S. T. Gille, and D. Menemenlis, 2016a: Mesoscale to submesoscale wavenumber spectra in Drake Passage. *J. Phys. Oceanogr.*, **46**, 601–620, <https://doi.org/10.1175/JPO-D-15-0087.1>.
- , S. T. Gille, T. K. Chereskin, and D. Menemenlis, 2016b: Seasonality of submesoscale dynamics in the Kuroshio Extension. *Geophys. Res. Lett.*, **43**, 11 304–11 311, <https://doi.org/10.1002/2016GL071349>.

- Smith, J. A., 2008: Vorticity and divergence of surface velocities near shore. *J. Phys. Oceanogr.*, **38**, 1450–1468, <https://doi.org/10.1175/2007JPO3865.1>.
- Torres, H. S., P. Klein, D. Menemenlis, B. Qiu, Z. Su, J. Wang, S. Chen, and L.-L. Fu, 2018: Partitioning ocean motions into balanced motions and internal gravity waves: A modeling study in anticipation of future space missions. *J. Geophys. Res. Oceans*, **123**, 8084–8105, <https://doi.org/10.1029/2018JC014438>.
- Wang, S., Z. Jing, H. Liu, and L. Wu, 2018: Spatial and seasonal variations of submesoscale eddies in the eastern tropical Pacific Ocean. *J. Phys. Oceanogr.*, **48**, 101–116, <https://doi.org/10.1175/JPO-D-17-0070.1>.
- Yu, X., A. L. Ponte, S. Elipot, D. Menemenlis, E. D. Zaron, and R. Abernathey, 2019: Surface kinetic energy distributions in the global oceans from a high-resolution numerical model and surface drifter observations. *Geophys. Res. Lett.*, **46**, 9757–9766, <https://doi.org/10.1029/2019GL083074>.
- Zhao, Z., 2017: The global mode-1 S2 internal tide. *J. Geophys. Res. Oceans*, **122**, 8794–8812, <https://doi.org/10.1002/2017JC013112>.